

Dune field pattern formation and recent transporting winds in the Olympia Undae Dune Field, north polar region of Mars

Ryan C. Ewing,^{1,2} Aymeric-Pierre B. Peyret,¹ Gary Kocurek,¹ and Mary Bourke^{3,4}

Received 13 October 2009; revised 22 February 2010; accepted 24 March 2010; published 28 August 2010.

[1] High-Resolution Imaging Science Experiment (HiRISE) imagery of the central Olympia Undae Dune Field in the north polar region of Mars shows a reticulate dune pattern consisting of two sets of nearly orthogonal dune crestlines, with apparent slipfaces on the primary crests, ubiquitous wind ripples, areas of coarse-grained wind ripples, and deflated interdune areas. Geomorphic evidence and dune field pattern analysis of dune crest length, spacing, defect density, and orientation indicates that the pattern is complex, representing two constructional generations of dunes. The oldest and best-organized generation forms the primary crestlines and is transverse to circumpolar easterly winds. Gross bed form-normal analysis of the younger pattern of crestlines indicates that it emerged with both circumpolar easterly winds and NE winds and is reworking the older pattern. Mapping of secondary flow fields over the dunes indicates that the most recent transporting winds were from the NE. The younger pattern appears to represent an influx of sediment to the dune field associated with the development of the Olympia Cavi reentrant, with NE katabatic winds channeling through the reentrant. A model of the pattern reformation based upon the reconstructed primary winds and resulting secondary flow fields shows that the development of the secondary pattern is controlled by the boundary condition of the older dune topography.

Citation: Ewing, R. C., A.-P. B. Peyret, G. Kocurek, and M. Bourke (2010), Dune field pattern formation and recent transporting winds in the Olympia Undae Dune Field, north polar region of Mars, *J. Geophys. Res.*, 115, E08005, doi:10.1029/2009JE003526.

1. Introduction

[2] Aeolian dune fields create some of the most striking patterns on Mars. Although the fluid/grain properties of the aeolian sediment transport system on Mars are different from those on Earth [Iverson and White, 1982], the robust, self-organizing nature of this complex system dictates that the emergence of dune field patterns on Mars will be much the same as on Earth [Werner, 1999, 2003; Kocurek and Ewing, 2005; Ewing and Kocurek, 2010b; Kocurek et al., 2010]. Martian patterns, like those on Earth, reflect the internal dune dynamics of self-organization and the geomorphic and climatic boundary conditions within which the dune field patterns evolve [Ewing and Kocurek, 2010a].

[3] One means of interpreting the geomorphic and climatic history of a dune field is through analysis of the dune field pattern [Tsoar et al., 1979; Lancaster et al., 2002; Ewing et al., 2006; Ewing and Kocurek, 2010a]. On Earth, dune field

pattern analysis via measurements from remote images of dune fields, statistical analysis of the measurements, and geomorphic observation has yielded robust interpretations of the evolution of regional-scale dune fields [Beveridge et al., 2006; Derickson et al., 2008]. This type of analysis is well suited to study the evolution of dune fields on Mars because the measurements and analysis are at the scale of the pattern (i.e., not the fluid/grain scale) and the measurements are taken remotely (i.e., no *in situ* data are required).

[4] The purpose of this study is to analyze in detail the dune field patterns of the Olympia Undae Dune Field in the north polar region of Mars in order to elucidate the most recent wind conditions and the dune field evolution. All dune crestlines and a representative sample of wind ripple crestlines within High-Resolution Imaging Science Experiment (HiRISE) [McEwen et al., 2007] image PSP_001432_2610 were measured and statistically analyzed to assess the spatial relationships of the dune field pattern in the center of Olympia Undae (160.3°W , 81.1°N ; Figure 1). Wind ripples were mapped to determine the flow fields of the most recent sediment transport event within the dune field. A model of the evolution of the pattern, which relates the spatial relationships of the pattern and the mapped flow fields, is developed and discussed in the context of the polar wind regime and regional, spatial changes within the Olympia Undae Dune Field pattern. This paper concludes that (1) the dune field pattern is complex (i.e., composed of two generations of dunes), the youngest pattern emerged with both easterly and

¹Department of Geological Sciences, The University of Texas at Austin, Austin, Texas, USA.

²Now at Division of Geological and Planetary Sciences, California Institute of Technology, Pasadena, California, USA.

³Planetary Science Institute, Tucson, Arizona, USA.

⁴School of Geography and the Environment, Oxford University Centre for the Environment, Oxford, UK.

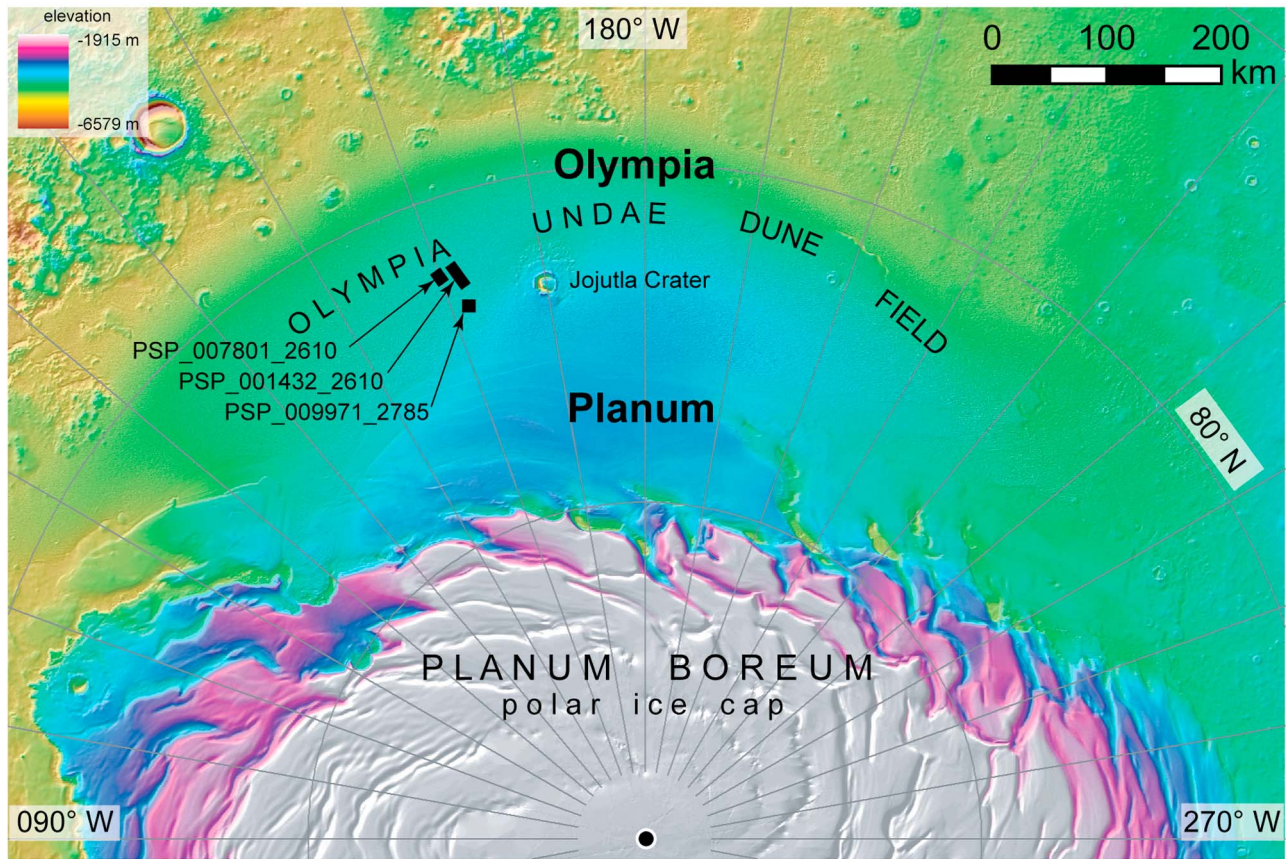


Figure 1. MOLA digital elevation model (DEM) of the north polar region of Mars centered on the Olympia Undae Dune Field. Note the elevation color ramp in the top left corner. HiRISE image PSP_001432_2610 (NASA/JPL/U of A) is the primary study area shown in detail in Figure 2. PSP_007801_2610 (NASA/JPL/U of A), shown in Figure 5, shows the seasonal defrosting of the dune field. PSP_009971_2785 (NASA/JPL/U of A) is shown in Figure 12 and is used as a comparison for the flow fields reconstructed within the study area.

northeasterly winds and is reworking the older pattern formed primarily by easterly winds; (2) the most recent transporting winds are from the northeast and are related to katabatic winds descending the north polar ice cap, Planum Boreum; (3) channelized katabatic winds from Olympia Cavi dominate the current state of dune field pattern development in the center of the field; and (4) the current pattern development occurs within an overall stabilized system through the accumulation of sediment by ice.

2. Motivation for Dune Field Pattern Analysis

[5] Two nearly orthogonal crestline orientations define the reticulate crestline pattern within the study area in the Olympia Undae Dune Field (Figure 2). Crestline orientation relates to the sediment-transferring wind regime, such that dunes orient to maximize the sediment transport perpendicular to the crestline (gross bed form-normal transport) [Rubin and Hunter, 1987]. Gross bed form-normal transport implies that, for a given wind regime, a simple crestline pattern emerges, which represents a single generation of dune construction [Kocurek and Ewing, 2005; Ewing et al., 2006]. A complex pattern (i.e., multigenerational) arises with the

superposition of multiple simple patterns and can be distinguished by multiple statistical populations of dune crestlines separated in scale or orientation. The reticulate pattern in the study area can represent either a simple pattern created under a single wind regime or a complex pattern composed of two generations of dune construction. In the former interpretation, the composite pattern would be classified as a star dune pattern created by a bimodal wind regime with a divergence angle between the dominant and subordinate winds of $\sim 90^\circ$ [see Rubin and Hunter, 1987, Figure 2; Werner and Kocurek, 1997, Figure 4; Kocurek and Ewing, 2005, Figure 4]. In the latter interpretation, each crestline trend formed under a different wind regime during separate constructional events. Quantitative analysis of the crestline pattern, along with geomorphic observation, provides a means to constrain the range of winds and constructional events that gave rise to the pattern in the Olympia Undae Dune Field.

3. Regional Geomorphic Context

3.1. The Olympia Undae Dune Field

[6] The Olympia Undae Dune Field is the largest sand sea in the north polar region of Mars, spanning from $\sim 120^\circ\text{W}$ –

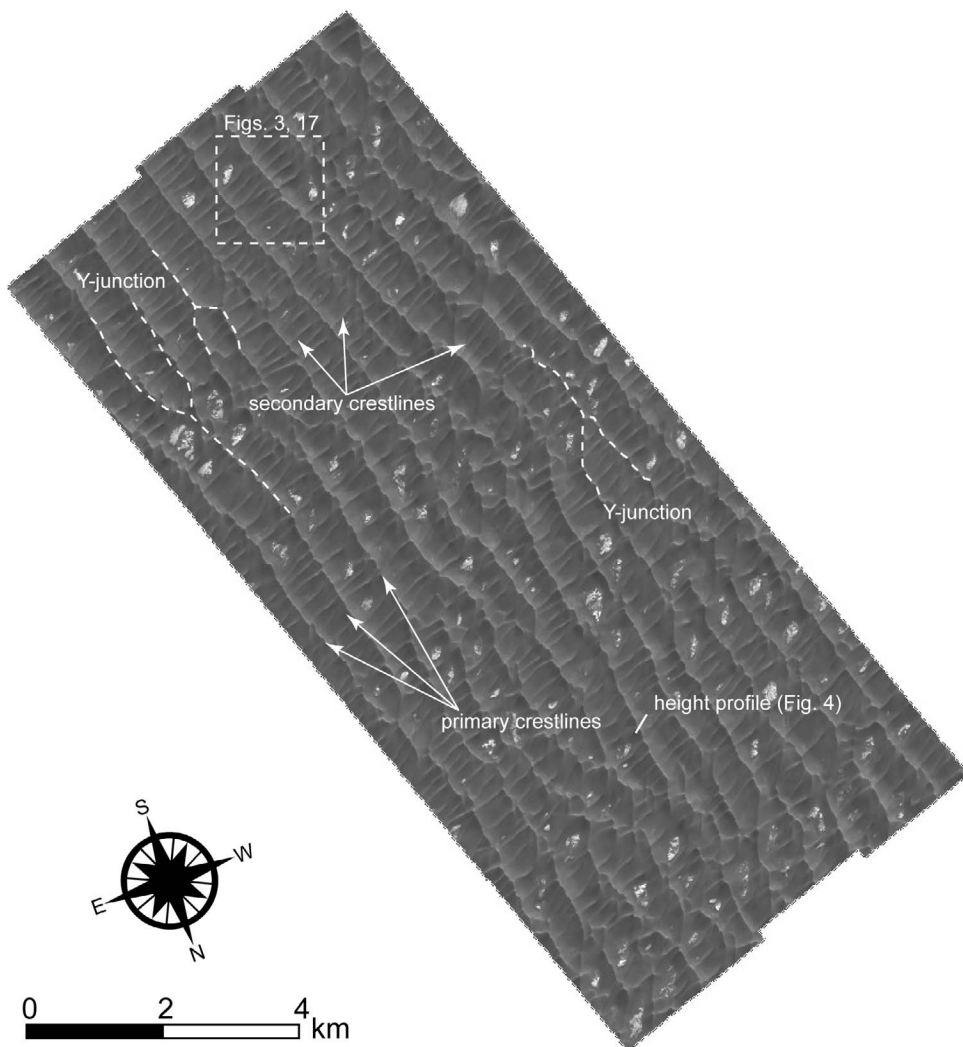


Figure 2. Study area: HiRISE image PSP_001432_2610 showing primary and secondary crestlines. Lighting is from 196°W longitude.

230°W and ~79°N–83°N [Tsoar *et al.*, 1979; Lancaster and Greeley, 1990; Tanaka *et al.*, 2005] with a total area of 385,000 km² [Hayward *et al.*, 2007]. The majority of the dune field mantles Olympia Planum, which is a large platform that rises nearly 800 m above the surrounding plains of Vastitas Borealis near the base of Planum Boreum (Figure 1).

[7] The Olympia Undae dunes have been primarily described and classified as crescentic ridges and barchan dunes. Crescentic ridges comprise the core of the field, and barchan dunes flank the southern and western margins [Tsoar *et al.*, 1979; Lancaster and Greeley, 1990; Tanaka and Hayward, 2008]. The dunes in the field center are thought to be mostly transverse to circumpolar easterly winds, whereas the dunes along the southern margin of the field appear to reflect a westerly wind belt [Tsoar *et al.*, 1979; Howard, 2000; Tanaka and Hayward, 2008].

[8] Estimations of the wind directions in Olympia Undae, based primarily on crestline orientation and slipface direction, indicate winds are largely from the east to the west with subordinate northeasterly winds in the western part of the field [Tsoar *et al.*, 1979; Tanaka and Hayward, 2008].

However, wind directions based on crestline and slipface orientation alone are not reliable indicators of wind direction, except in the case of a dominantly unidirectional wind regime. Because crestlines are oriented to be as perpendicular as possible to all constructive winds (i.e., gross bed form-normal transport of Rubin and Hunter [1987]), in nonunimodal wind regimes, the crestline orientation shows the direction of net bed form migration but not directly the constructive wind directions that cause the crestline orientation. For example, a crescentic dune crestline may be transverse (i.e., the incidence angle between the crestline and the resultant transport vector is between 75° and 90° [Hunter *et al.*, 1983]) under a bimodal wind regime in which the divergence angle between dominant and subordinate winds are between 0 and ~70° [see Rubin and Hunter, 1987, Figure 2; Kocurek and Ewing, 2005, Figure 4]. Thus, a dune crestline may be transverse to the resultant transport direction but not to the constructive winds. The interpretation of an east-to-west wind direction in Olympia Undae based on the crescentic dune morphology may be oversimplified. The apparent dispersion direction of gypsum detected within the dune field from the east to west

[*Langevin et al.*, 2005] substantiates the net transport wind direction indicated by the orientation of the dune crestlines but does not provide any further details of the wind regime. Katabatic winds from the north and northeast, descending off Planum Boreum, have been interpreted from frost streaks and constitute an additional component of the wind regime in Olympia Undae [*Tsoar et al.*, 1979; *Howard*, 2000; *Tanaka and Hayward*, 2008].

[9] The dunes of Olympia Undae are thought to be mostly inactive, stabilized features [*Breed et al.*, 1979; *Schatz et al.*, 2006; *Feldman et al.*, 2008; *Tanaka et al.*, 2008]. Based upon a model that used Mars Odyssey Neutron Spectrometer data, *Feldman et al.* [2008] suggested that the bulk of the dune volume is stabilized by ice (i.e., niveo-aeolian) deposited through water vapor diffusion into the sediment pore space or through the entrainment of ice precipitation and that a thin (~10 cm) more mobile layer of sediment mantles the stabilized portion of the dunes. Their model is supported by a surface morphology that includes surface fractures, steep-walled pits, the apparent absence of grainflow avalanches, and an overall topographically subdued crestline appearance. Dune inactivity in Olympia Undae is further supported by time series observations from Viking and Mars Orbiter Camera imagery made by *Schatz et al.* [2006], who found no evidence of dune movement over 4–15 Martian years in both the equatorial latitudes and in the north polar region in Chasma Boreal. Although no dune movement is observed, some sediment mobility is implied by sand streaks, which emanate from the horns of barchan dunes [*Tanaka et al.*, 2008] and in three instances, the erosion and disappearance of small dome dunes [*Bourke et al.*, 2008; 2009].

[10] Dark dune sediments thought to be composed of basaltic andesite or weathered basalt comprise nearly all of Olympia Undae [*Bandfield et al.*, 2000; *Wyatt et al.*, 2004; *Fishbaugh et al.*, 2007]. Gypsum comprises a secondary component of the dune mineralogy and ranges in concentration up to 24% near the eastern margin of the dune field and decreases westward [*Langevin et al.*, 2005; *Fishbaugh et al.*, 2007; *Horgan et al.*, 2009a]. The dune crests show the highest concentrations of gypsum, with lesser amounts occurring on the dune slopes and in the interdune areas [*Roach et al.*, 2007; *Horgan et al.*, 2009a; *Lahtela et al.*, 2009].

[11] Sedimentary deposits that flank and underlie much of the polar ice cap are thought to be the source for the dune sediments [*Byrne and Murray*, 2002; *Fishbaugh and Head*, 2005; *Tanka et al.*, 2008]. Recent detailed mapping of these deposits indicates that much of the dune sediment has eroded from the middle Amazonian, Planum Boreum cavi unit [*Tanka et al.*, 2008]. Primarily exposed along slipfaces near the base of the North Polar Layered Deposits in Olympia Cavi, the cavi unit makes up the majority of Olympia Planum, upon which Olympia Undae sits. In outcrop, the cavi unit appears as dune cross-bedded strata, interbedded with polygonally fractured ice layers, and is interpreted as an ancient aeolian sand sea, which coevolved with deposition of ice [*Byrne and Murray*, 2002; *Fishbaugh and Head*, 2005; *Herkenhoff et al.*, 2007; *Tanaka et al.*, 2008].

3.2. Geomorphology of Study Area

[12] The area within the Olympia Undae Dune Field chosen for the dune field pattern analysis covers 93 km² and

is centered at 160.3°W, 81.1°N (Figure 1). This area lies near the center of the Olympia Undae Dune Field, 80 km east of Jojutla Crater and 200 km south from the base of Planum Boreum.

[13] Six distinct morphologic features give rise to the dune field pattern within in the study area: (1) NNW trending crestlines form the largest, primary set of dunes that extend the length of the study area (Figure 2). (2) A smaller, secondary set of NE trending crestlines are oriented nearly perpendicular to the primary crestlines (Figures 2 and 3). At the dune scale, (3) apparent slipfaces are present along the primary dune crests (Figures 3 and 4), (4) wind ripples are ubiquitous over nearly all sediment-covered surfaces of the dune field (Figure 3b), and (5) more widely spaced coarse-grained wind ripples occur within the interdune areas and on the eastern slopes of the primary dunes (Figure 3b). (6) The substrate underlying the dunes is exposed in interdune areas that are not covered by sediment (Figures 2, 3, and 7b).

3.3. Primary Dunes

[14] The largest-scale dunes within the study area are straight crested and regularly spaced. The dune slopes and crests are subdued in appearance, only becoming sharp at the brink of the apparent slipfaces that occur along the crestlines. The basic element of the crests extends over the length of the image, giving rise to a continuous appearance with Y junctions, typical of well-organized linear dunes and wind ripples (Figure 2). In detail, however, disconnections occur where the crests are offset, typically where they are intersected by secondary crests or slipfaces (Figure 3a). *Feldman et al.* [2008] estimated dune heights within a nearby area (78.0°N, 303.9°E) in Olympia Undae at 75 m. Height estimates in this study range from 10 to 20 m based upon the reconstructed flow fields (see below) and 65 m based on a photoclinometry profile (Figure 4a). Dune profiles show the primary dunes have a slight asymmetry, with the steepest slopes occurring on the western side of the crestlines (Figure 4a). From this profile, the W facing slopes are interpreted as the primary lee slope of the dunes, and the E facing slopes are the primary stoss slope, which implies a general transport direction from the east to the west.

[15] Profile measurements were extracted by a simplified photoclinometric procedure that assumes uniform albedo along a profile line and Lambertian photometric properties of the surface (i.e., brightness is only dependent on the solar incident angle) [see *Bourke et al.*, 2006; *Zimbelman*, 2010]. Although the albedo of the dune surface appears uniform across the profiles, this method does not account for differences in surface mineralogy that may alter the surface brightness. Gypsum, which is most concentrated at the dune crests in Olympia Undae [*Roach et al.*, 2007; *Horgan et al.*, 2009a], may introduce non-Lambertian properties to the dune surface that cause higher-than-expected slope values. Because of the method assumptions, the heights derived from slopes are considered maximum values and are intended as exploratory data.

3.4. Secondary Dunes

[16] The secondary dunes are rounded, topographically subdued features that extend nearly perpendicular to and are bound by the primary crestlines. Height profiles could not be extracted from these dunes using the photoclinometric

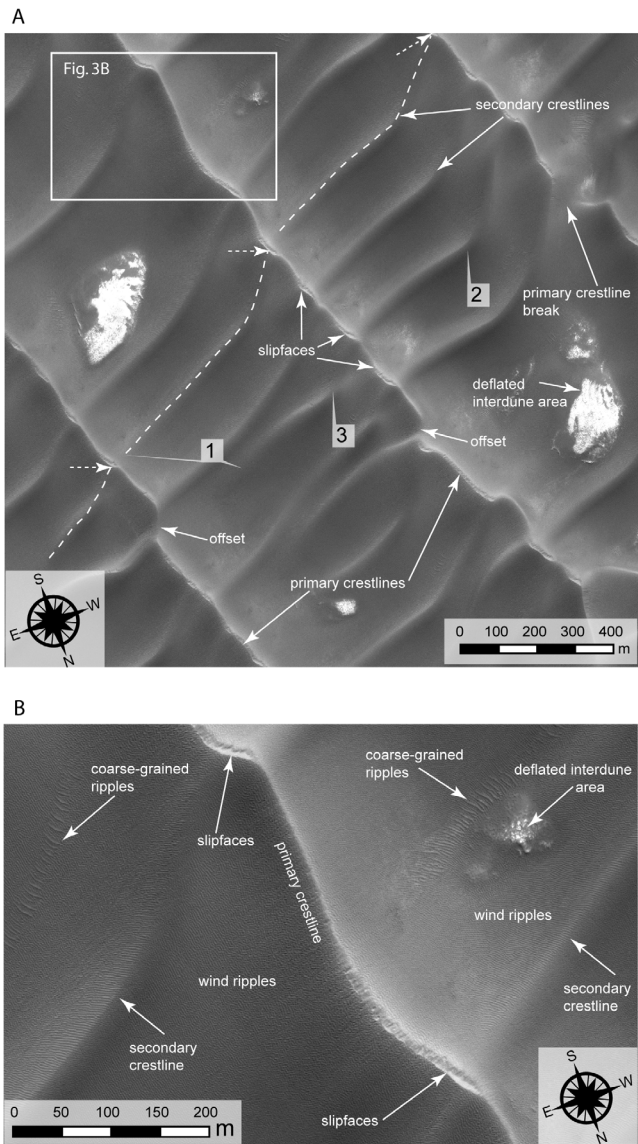


Figure 3. Detail images showing the geomorphic elements of the study area. (a) Inset located in Figure 2. Lighting is from 196°W. 1 indicates an unattached eastern termination of a secondary dune. 2 indicates a bend in the secondary crest line. 3 shows a secondary dune that is unattached at both the eastern and western terminations. The dashed white lines follow the alignment of three secondary crestlines across three primary dunes. (b) Inset from Figure 3a showing all the geomorphic features that make up this dune field pattern.

method because the dune orientation is nearly parallel to the solar azimuth angle. Without a height profile, presence of a distinct stoss and lee slope cannot be determined from dune asymmetry; however, based upon ripple orientations the SE facing slopes appear to be the lee slopes. Although these crestlines are not connected to each other, they typically align across the primary crestlines, giving rise to the reticulate pattern (Figure 3a). The secondary dunes most commonly extend up the eastern slopes of the primary dunes, typically deflected southward as they approach the primary crestline

and terminate where they intersect the crestline of the primary dunes (Figure 3a). In contrast, the eastern terminations of the dunes are usually unattached to the primary crestlines and terminate at the base of the western lee slopes of the primary dunes or within the interdune areas (Figure 3). Less common are secondary crestlines that remain entirely unattached at both their eastern and western terminations (Figure 3).

3.5. Slipfaces

[17] The subdued appearance of the primary crestlines is broken quasiperiodically in the along-crest direction by scarps, which commonly form at the intersection of the secondary and primary crestlines (Figure 3). These features are typically arcuate in shape, with a wider, steeper center that tapers in the along-crest directions. Similar features were described as elongate depressions by Feldman et al. [2008]. Based upon the sharp brink, the striated appearance of the scarp surface and on evidence presented below that these features are transverse to one dominant wind direction, these scarps are interpreted to be depositional slipfaces.

[18] The slipfaces themselves shallow downslope and terminate at a rampart (Figures 4a and 4b), beyond which the dune slope is covered with degraded wind ripples (Figure 3b). Grainflow, which would be expected on a depositional slipface, may be represented by the downslope-striated structures, but distinct grainflow lobes are not apparent possibly because they are (1) below the resolution of the image, (2) not recently active, or (3) indurated, eroded, and oversteepened.

3.6. Wind Ripples

[19] Ripples are omnipresent within the dune field except on the slipfaces and within the deflated interdune areas (Figure 3b). The majority of the ripples appear well organized with typical Y junctions and continuous crestlines. The ripples change orientation in a systematic way related to their position on the primary and secondary dunes, which corresponds to the dune-induced secondary airflow over the dune field (see below). Where the secondary airflow patterns should intersect, the ripples are more discontinuous and ripple interference patterns appear.

[20] Although nearly the entire dune field is covered with ripples, the ripples on the SE facing slopes of the secondary dunes are the most active appearing within the field (Figures 3b and 5a). These ripples are far more distinct and have more continuous crestlines than other ripples in the adjacent area (Figure 5a). In addition, ripples on the SE facing slopes truncate surface fractures, which appear on the NW facing slopes of the secondary dunes (Figure 5a). In contrast, the wind ripples on the NW facing slopes of the secondary dunes are subdued, discontinuous, and truncated by the surface fractures (Figure 5a). Feldman et al. [2008] interpreted similar surface fractures as indicators of the cohesion of the surface sediments and tensional stresses related to the presence of subsurface ice.

[21] The apparent greater mobility of the ripples on the SE facing slopes of the secondary dunes may be related to the stability of the near-surface ground ice on Mars. Aharonson and Schorghofer [2006] show that the stability of near-surface ice on Mars depends upon local slope. In the Northern Hemisphere, ice is more stable on N facing slopes, which receive less sunlight than do the S facing slopes. The SE facing slopes of the secondary dunes appear to defrost

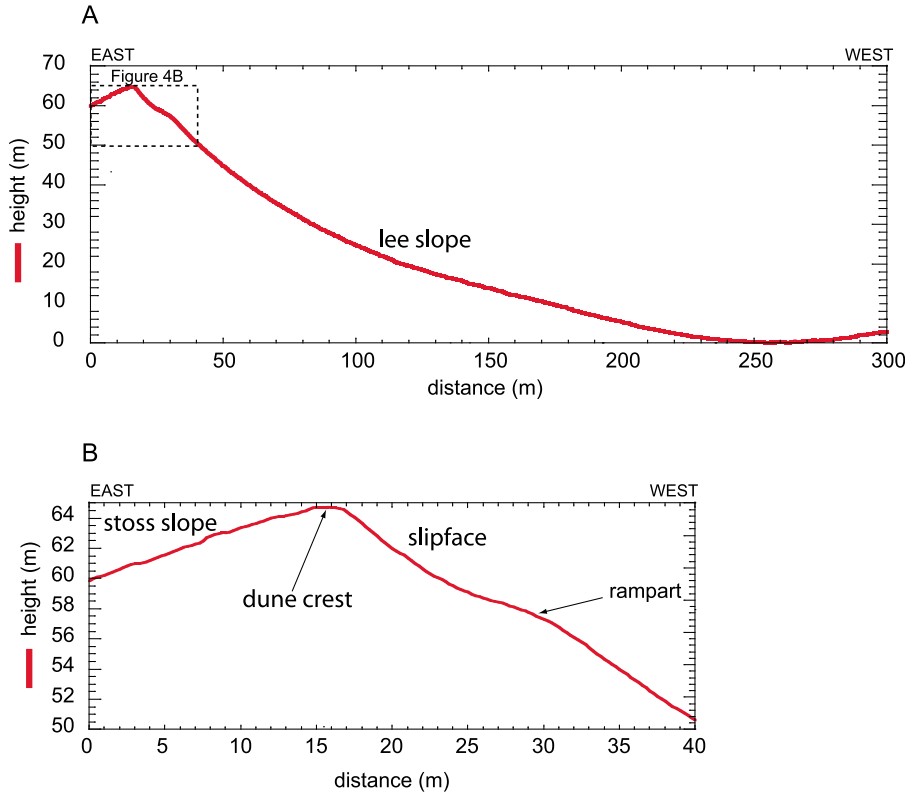


Figure 4. (a) Height profile across a primary dune crestline using a simplified photoclinometric method (location shown in Figures 2 and 7b) [see Bourke et al., 2006; Zimbelman, 2010]. The left Y axis shows the dune height (thick, solid red line), which should be considered a maximum using this method (see text for discussion). The asymmetry of the dune suggests that the shallow-sloped E side is the stoss slope and that the steep, western slope is the lee. (b) Note the steepest slopes occur near the dune crest at the apparent slipfaces.

earlier during the Martian spring (Figures 5b and 5c), which is consistent with receiving greater amounts of sunlight, and in turn, less stable near-surface ice. If ice is the dominant dune sediment cement, the near-surface sediment on the SE facing slopes of the secondary crestlines may defrost to a greater depth and be available for aeolian transport for a greater percentage of the time than the surrounding sediment, thus accounting for the apparent greater activity of ripples on these slopes. In contrast, the NW facing slopes may remain mostly frozen and preferentially form the surface fractures. Feldman et al. [2008] also suggested that aspect-related high insolation receipts may explain the location of the H₂O minima in Olympia Undae as well as the formation of sublimation pits along dune crests.

3.7. Coarse-Grained Ripples

[22] Ripples, which are more widely spaced (3–8.2 m) than the ubiquitous wind ripples (1.6–2.6 m), occur within the interdune areas between the primary crestlines and on the E facing slopes of primary dunes between secondary dunes (Figures 3 and 7c). These ripple crestlines display less variability in orientation and commonly deviate from the orientation of nearby smaller wind ripples. On Earth, the presence of two distinct scales of ripples within an interdune area typically indicates that the ripples emerged from a strongly bimodal grain size population. The larger, more widely

spaced ripples comprise the coarser fraction of sand and the surrounding smaller ripples comprise of the finer, more abundant sand fraction [Bagnold, 1941, p. 155; Fryberger et al., 1992; Jerolmack et al., 2006]. The presence of two scales of ripple wavelengths suggests a spatial sorting of the grains within this area of Olympia Undae. The concentration of coarser grains most likely represents a deflated lag where the finer grains have been removed.

3.8. Interdune Areas

[23] The interdune areas host a variety of geomorphic features related to the evolution of the dune field. Polygonal fractures are visible in many of the interdune areas and likely indicate the presence of ice [Feldman et al., 2008]. Most notably, however, are the arcuate ridges (Figure 6), which appear to consist of the same material as the underlying substrate and, in another location within Olympia Undae (78.0°N, 303.9°E), have been interpreted as barchan dune cross strata [Feldman et al., 2008]. In the study area, these arcuate ridges can be clearly distinguished as large sets of aeolian dune cross strata created by some type of crescentic dune (Figures 6b–6d). Although the concave-westward curvature of the cross strata indicates the dune migration was similar to the general, inferred migration direction of the primary dunes, as based upon their asymmetry (Figure 4), the shape of the cross strata does not match well with the

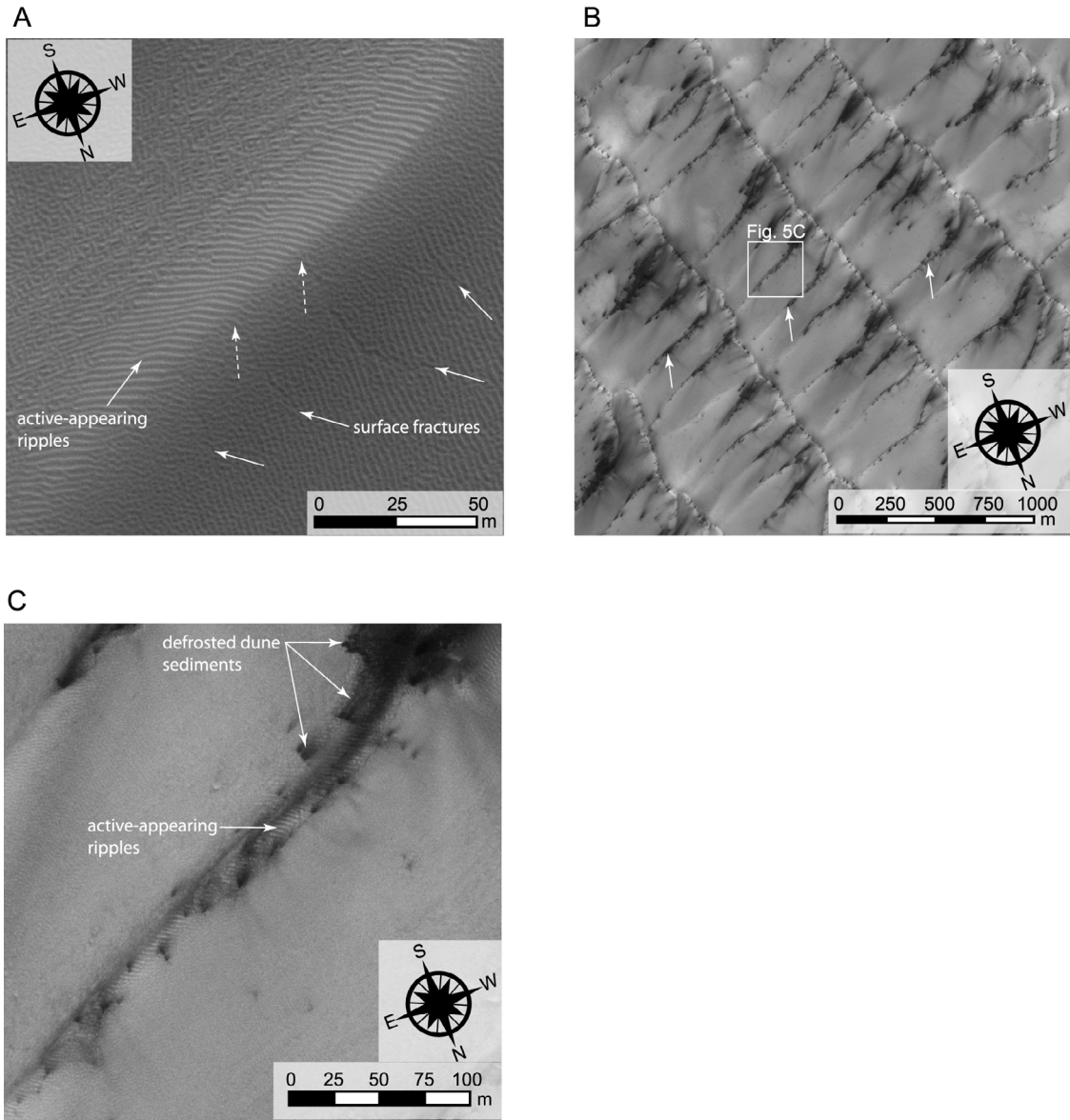


Figure 5. (a) Image within the study area showing active-appearing ripples on the SE facing slopes of the secondary dunes (see text for discussion). Surface fractures on the NW facing slopes of the secondary dune are indicated by the dashed white arrows. (b) HiRISE image PSP_007801_2610, which is adjacent eastward of the study area (location shown in Figure 1), showing spring defrosting of dunes. The white areas are frost, and the dark areas are exposed dune sediment. Note that the SE facing slopes of the secondary crestlines are defrosting first (white arrows). (c) Subset of Figure 5b showing the defrosted active-appearing ripples on the SE facing slope of the secondary dunes. The early thawing of the SE facing slopes suggests that the sediment on these slopes may less stabilized by ice and more available for aeolian transport.

crestline shape of the current dunes. These truncated sets of cross strata probably are outcrops of the underlying Planum Boreum cavi unit [Tanaka *et al.*, 2008].

4. Methods

[24] Every dune crestline and slipface brink and a representative sample of ripple crestlines were manually digitized from HiRISE image PSP_001432_2610 using geographical information system (GIS) software (Figure 7). Dune and

ripple crest spacing, crestline length, and defect density were measured using GIS. Defect density is $\rho = N/L$, where ρ is the defect density, N is the number of defect pairs (pairs of dune terminations), and L is the total crestline length within the field [Werner and Kocurek, 1999]. Primary and secondary crestlines and slipfaces were digitized at a scale of 1:2000. Coarse-grained and fine-grained wind ripples were measured at 1:500. Crestlines that extend outside of the study area were not digitized. Where a break in the primary crestline occurs and is greater than ~50 m, the crestlines were terminated (see

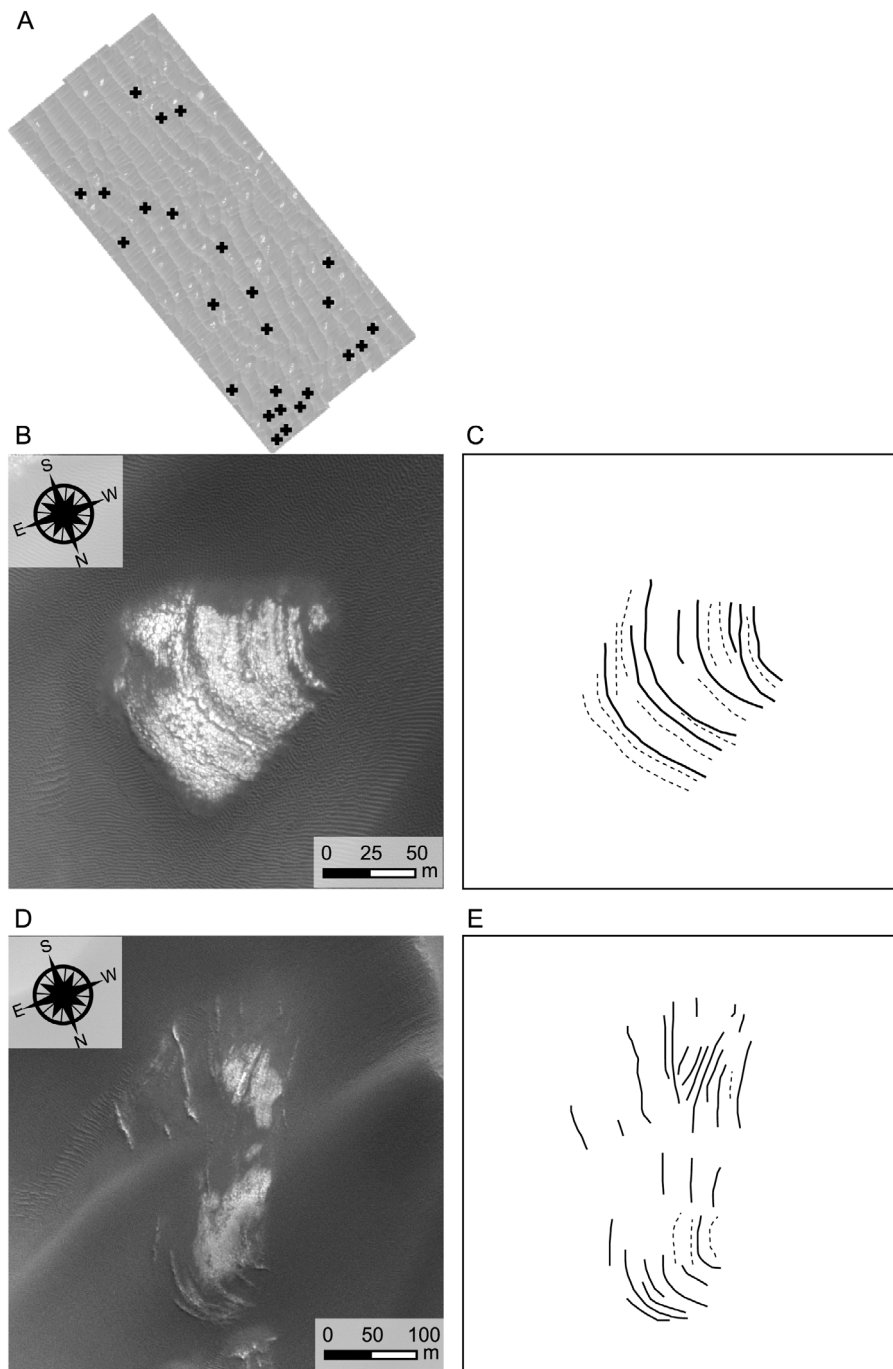


Figure 6. (a) Location of all arcuate ridges interpreted as aeolian dune cross-strata exposed within the study area. (b and d) Examples of the cross-strata. (c and e) Lines traced along the cross strata. The solid lines indicate the most prominent ridges; dashed lines indicate smaller ridges. Note that the curvature of the cross strata indicates a migration direction to the WSW similar to the inferred migration direction of the primary crestlines based on dune asymmetry.

Figure 3a). Breaks in the primary crestline were defined as portions of the crestline where the crest (i.e., a change from a positive to a negative slope) could not be clearly defined at the scale of digitization. Crestline breaks typically appear as troughs that offset the trend of the primary crest and coincide with the intersection of a secondary crestline and a slipface. Slipface brink were measured as part of the primary crestlines, as well as analyzed individually.

[25] Spacing was measured along transects perpendicular to the primary, secondary, coarse-grained, and wind ripple crestlines. Spacing between slipfaces was measured as the distance from midpoint to midpoint of each slipface along the primary crestline on which they occur. Defect density is a field-scale measurement and was determined for each set of crestlines. Dune, slipface, and ripple crestline orientations were measured as straight lines between crestline terminations

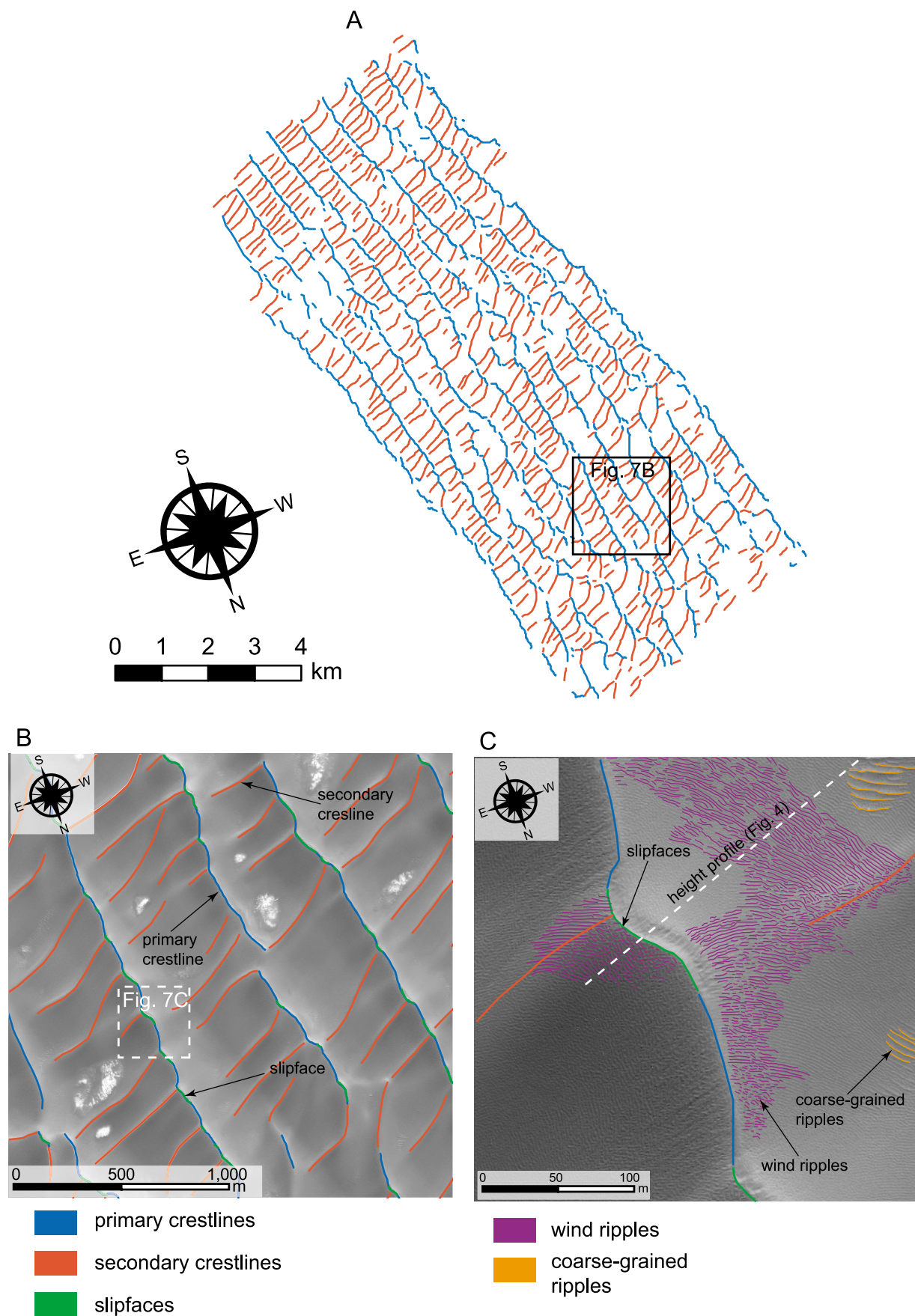


Figure 7

Table 1. Statistical Summary of Dune Field Pattern Measurements

	Primary Crestlines	Secondary Crestlines	Slipfaces	Coarse-Grained Ripples	Ripples
Crest length (m)					
Count (<i>n</i>)	372	587	670	313	966
Mean	360	386	62	28	10
Median	217	389	52	27	6
Standard deviation	425	153	40	12	11
Coefficient of variation	1.18	0.40	0.65	0.45	1.11
Spacing (m)					
Count (<i>n</i>)	103	407	536	240	205
Mean	637	215	199	5.6	2.1
Median	640	187	187	4.9	2.2
Standard deviation	133	89	93	2.6	0.5
Coefficient of variation	0.21	0.42	0.47	0.46	0.22
Defect density	0.0027	0.0026	0.016	0.035	0.099

and plotted as rose diagrams. Because nonlongitudinal line orientations near the pole may change significantly over relatively short distances, the azimuth orientation relative to north for lines greater than 500 m was calculated along 500 m line segments and averaged over the total number of line segments along the line. The maximum line orientation errors of a 500 m line between 79°N and 83°N latitude, which is the range of latitudes for the Olympia Undae Dune Field, are between $\sim 0.05^\circ$ and $\sim 0.1^\circ$.

5. Spatial Relationships in the Dune Field Pattern

5.1. Dune Field Pattern Measurements

[26] The digitized primary and secondary dune crestlines are shown in Figure 7a. Figure 7b shows the digitized crestlines overlain on a portion of the HiRISE image. Figure 7c shows a sample of the digitized coarse-grained and ripple crestlines overlain on the HiRISE image. Measurements from these features are summarized in Table 1.

[27] The distributions of dune and ripple crestline and slipface brink lengths and spacing data were analyzed statistically using cumulative log probability plots following the methods of Ewing *et al.* [2006] (Figures 8a and 8b). This type of analysis provides a simple statistical basis by which the pattern morphologic features can be compared and from which the relative age, organization, and events that gave rise to the pattern can be interpreted. These plots can be related to observations and models of dune field pattern development on Earth, which indicate overall pattern organization increases with time [Werner and Kocurek, 1999; Ewing *et al.*, 2006]. Older patterns are greater in spacing and crest length and lower in defect density than younger patterns, and in older pattern populations, the variability among these parameters is less than that of younger populations.

[28] Because of their distinct morphologic character (i.e., ripples, dunes, and slipfaces), each feature was plotted as a separate population. In these plots, a single lognormally distributed population is represented by a straight-line segment of data [Sinclair, 1976]. The median value of the data is at the 50th percentile, and the variability of the data is related

by the slope of data trend, such that the lower the slope, the smaller the variability. Numerically, the degree of variability in each population is related by the coefficient of variation, which is the ratio of the standard deviation over the mean ($C_v = \sigma/\mu$) (Table 1).

[29] Figure 8a shows the cumulative log frequency plots for the spacing data. The primary crestlines have the highest median and mean spacing values of all the data ($\mu_{\text{primary}} = 637$ m) and the data plot as nearly a flat line, indicating a low degree of variability in the population. The secondary crestlines and the slipfaces have the same median spacing value at 187 m and overall nearly identical distributions of spacing values ($\mu_{\text{secondary}} = 215$ m, $\mu_{\text{slipface}} = 199$ m). The coarse-grained ripple data show higher spacing values ($\mu_{\text{coarse}} = 5.6$ m) and a higher degree of variability than the wind ripples ($\mu_{\text{fine}} = 2.1$ m). All spacing data curves plot as straight-line segments, indicating that each represents a distinct lognormally distributed population.

[30] Figure 8b shows the cumulative log frequency plots for crest length. Although the primary crestlines are the dominant morphologic feature in the study area and have a highly organized and continuous appearance at the scale of the HiRISE image (Figures 3a and 7a), the crest lengths of the primary crestlines are highly variable, ranging over at least 2 orders of magnitude ($\mu_{\text{primary}} = 360$ m). The lower range of values represent primary crestlines that are disrupted or broken by secondary crestlines and slipfaces. At the higher range of values, greater crest lengths are not represented because they extend beyond the image. The secondary crestlines are less variable in length and have median and mean values ($\mu_{\text{secondary}} = 386$ m), which are greater than that of the primary crestlines. The secondary crestline data are strongly top truncated, which is indicated by the flattening of the data curve at the higher values. The top truncation of the data values may arise because the distribution of the secondary crest length population is approaching a uniform distribution, which on this plot type creates a strongly top-truncated data curve. The slipface brink lengths ($\mu_{\text{slipface}} = 62$ m) and coarse-grained ripples ($\mu_{\text{coarse}} = 28$ m) show a moderate degree of

Figure 7. (a) Digitized primary dune and secondary dune crestlines and slipface brinks. (b) Digitized crestlines overlain on the study area HiRISE image. Location of image shown in Figure 7a. (c) Digitized coarse-grained and wind ripple crestlines overlain on inset of Figure 7b. Note the change in orientation of the ripples with respect to the primary and secondary crestlines.

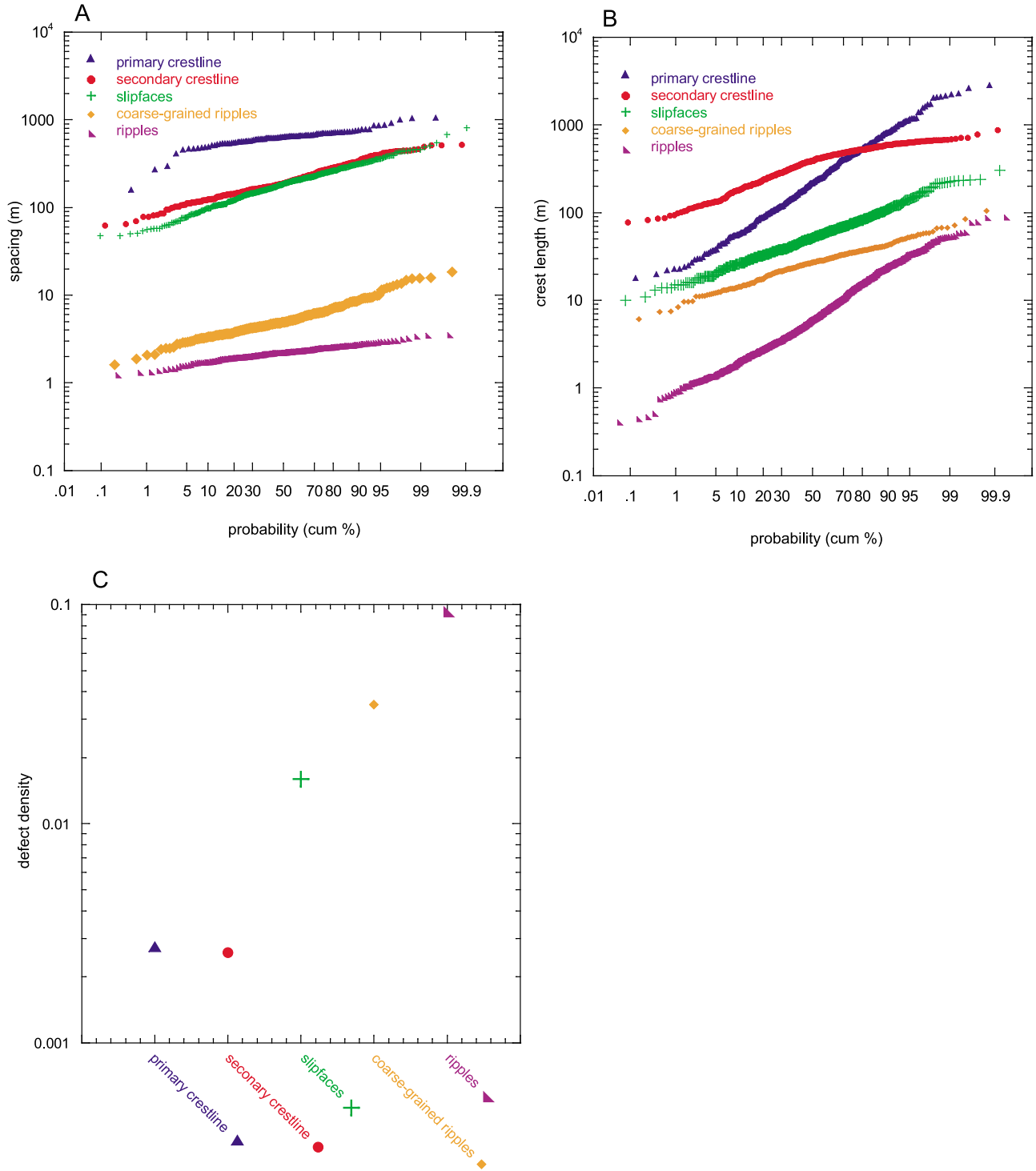


Figure 8. Cumulative log-probability plots showing the distributions of (a) crestline spacing and (b) crest length. (c) Defect density values for each crestline population (see text for discussion).

variability, whereas the ripple crestline lengths ($\mu_{\text{fine}} = 10 \text{ m}$) are highly variable, ranging over 2 orders of magnitude.

[31] Figure 8c shows the defect density for each crestline population. The primary crestlines ($\rho_{\text{primary}} = 0.0027$) and the secondary crestlines ($\rho_{\text{secondary}} = 0.0026$) show nearly the same values. The coarse-grained ripples ($\rho_{\text{coarse}} = 0.035$) have a lower defect density than the wind ripples ($\rho_{\text{fine}} =$

0.099), and the values of the slipfaces ($\rho_{\text{slipface}} = 0.16$) fall below that of the coarse-grained ripples and above that of the primary crestlines.

[32] Figures 9a–9e show the range of dune and ripple crestline and slipface orientations as rose diagrams. The orientation values are reported relative to north. The orientations of the primary (342°) and secondary (060°) crestlines are

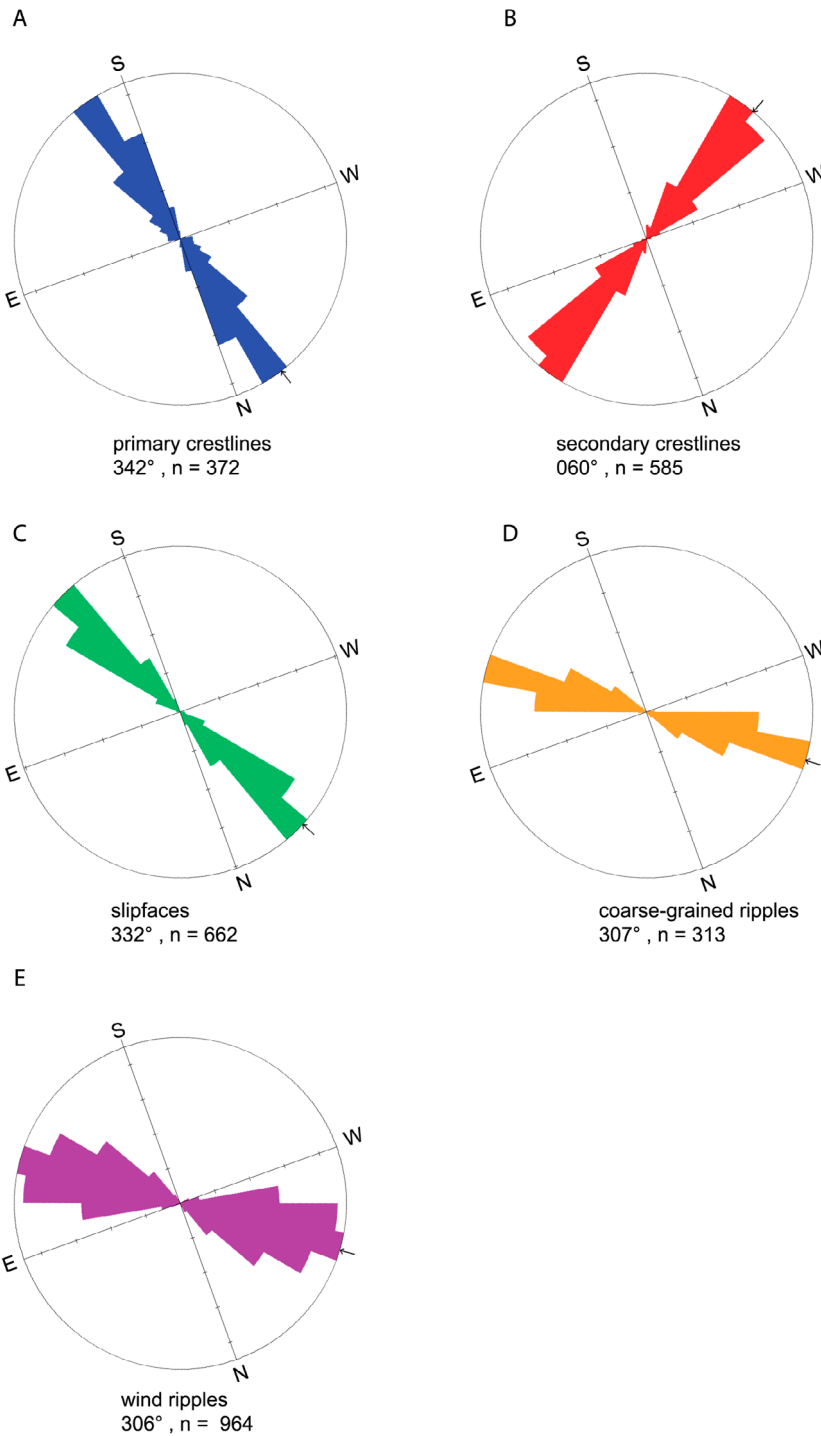


Figure 9. Rose diagrams of crestline orientation for (a) primary crestlines, (b) secondary crestlines, (c) slipfaces, (d) coarse-grained ripples, and (e) wind ripples. North is 0 with azimuth values increasing in the clockwise direction. The mean orientation value and the total number of measurements are indicated beneath each rose diagram.

nearly perpendicular. The slipface orientations (332°) trend closely with the primary crestlines. Although locally different, the mean trends of the coarse-grained ripples (307°) and fine-grained ripples (306°) are the same, indicating formation in the same wind regime and supportive of the interpretation that they represent a lagged concentration of coarse grains.

5.2. Spatial and Geomorphic Relationships of the Pattern

[33] The measured spatial relationships in the pattern variables along with geomorphic evidence indicate that (1) the primary dunes are older and less active than the secondary

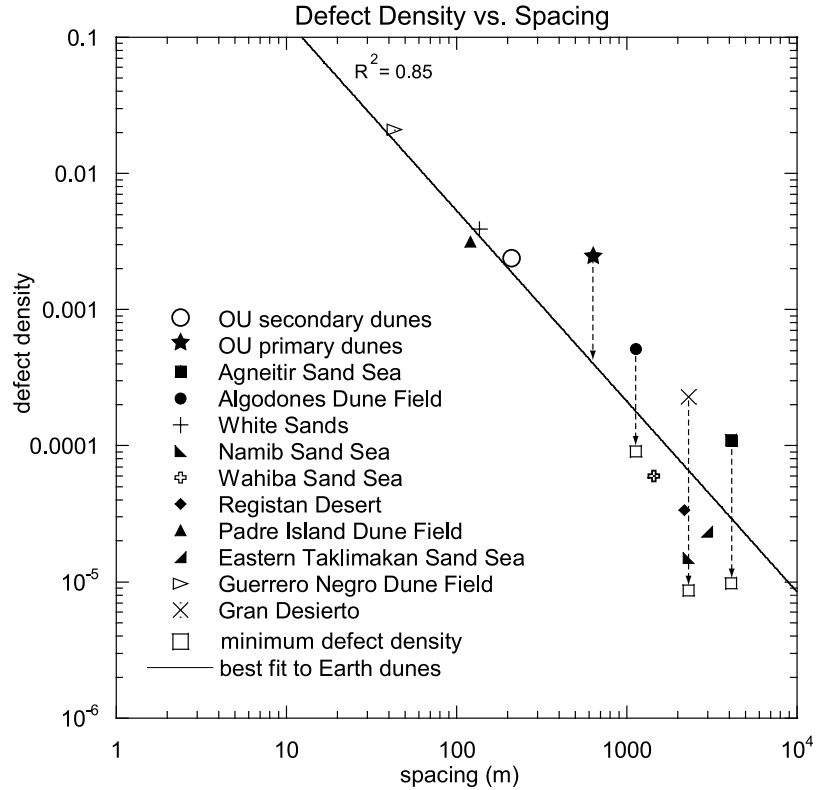


Figure 10. Plot showing defect density versus spacing for 10 dune fields on Earth and the primary and secondary dunes measured in the Olympia Undae Dune Field (OU). The OU primary dunes have a higher defect density than expected for the measured spacing, which suggests that the pattern is being broken. The dashed arrow from OU primary dunes projects the defect density to the trend determined from Earth dunes. The three Earth dune fields that deviate from the trend have been degraded. The open boxes indicate their relict defect densities [cf., Ewing and Kocurek, 2010a].

dunes, (2) the secondary dunes and slipfaces coevolved, (3) the secondary dunes and slipfaces are breaking up the primary dune pattern, and (4) the spacing between the primary dunes is an areal limit boundary condition to the evolution of the secondary dunes.

[34] The primary dunes have the greatest mean spacing and a very narrow range of spacing values, which suggests these dunes are highly evolved and represent the oldest pattern in the study area [Kocurek *et al.*, 1992; Werner and Kocurek, 1999; Ewing *et al.*, 2006]. In contrast, the range of primary dune crest lengths spans at least 2 orders of magnitude, indicating a poorly organized pattern, which is reflected in the relatively high defect density. This contrasting state of pattern organization (i.e., spacing versus crest length and defect density) is well illustrated in Figure 10, in which defect density is greater than expected for dunes with this spacing. By analogy with Earth examples [Ewing and Kocurek, 2010a], the greater defect density occurs as the primary dunes are reworked and segmented, as evident in Figures 3a and 7a.

[35] The nearly identical distributions of the secondary dune and slipface spacing measurements suggest that the formation of these features is related (Figure 8a), an interpretation supported by geomorphic observations. (1) Slipfaces typically occur where the western terminations of the secondary dunes intersect the primary dune crestlines (Figures 3a and 3b). (2) The eastern terminations of the secondary dunes typically occur below a slipface (Figures 3a and 3b). (3) The

secondary crestlines and slipfaces typically align across the primary crestlines (Figures 3a and 3b). The measurements and observations reasonably argue that the intersection of the secondary dunes with the primary crestlines causes the slipfaces to develop and the development of a slipface initiates the development of a secondary crestline in the lee of the primary dunes. In both cases, the development of the slipfaces and the secondary crestlines is breaking up the primary crestlines.

[36] The values within the top-truncated portion of the secondary dune crest length population are nearly the same as the mean spacing of the primary dunes (Figures 8a and 8b). This relationship suggests that the primary dune spacing creates an areal limit on the crest length development of the secondary dunes [Ewing and Kocurek, 2010a]. The top truncation and the uniform distribution arise because the secondary dunes can only grow to the limit of the spacing between the primary dune crestlines, which creates a population in which the secondary dune crest lengths are the same as primary dune spacing. This relationship provides additional evidence that the secondary dunes are younger features than the primary crestlines and is consistent with the secondary dunes breaking up the primary dune crests.

[37] Overall, the dune field pattern is best described as a complex pattern. The primary dunes emerged first, and during a later episode of pattern construction, the secondary dune pattern developed. The highly organized state of the

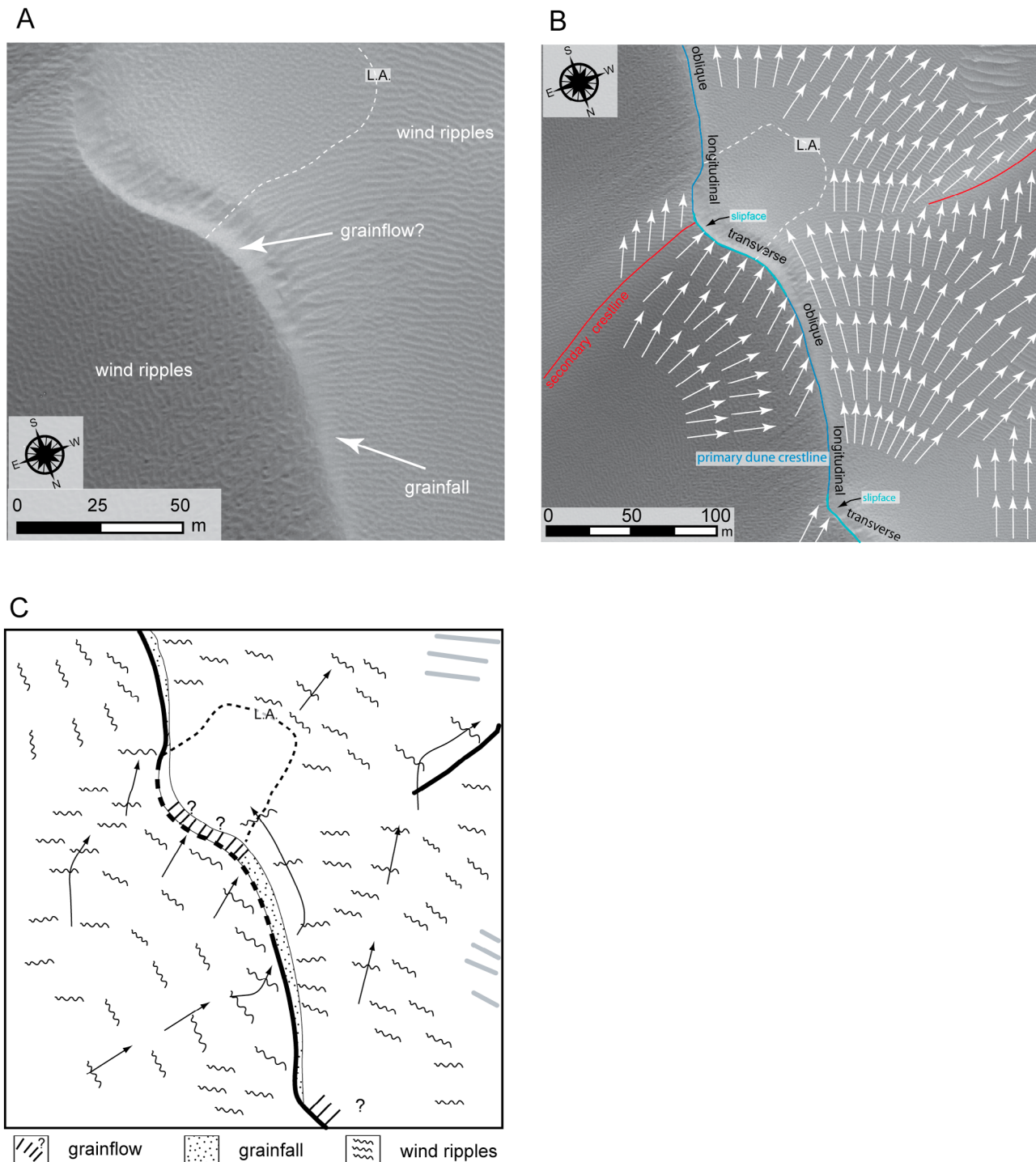


Figure 11. Characterization of the secondary flow field within the study area. (a) Part of the crestline shown in Figure 11b, showing the surface features arising from the dune-modified secondary airflow. Note the mottled ripples in the lee of the slipface and within the line of attachment (L.A.). Evidence of grainfall appears as a bright dusting along the western side of the primary crest that obscures the eastern terminations of the wind ripples that appear downslope. The grainfall apron widens along-slope southward until it merges with the slipface. Note the apparent absence of grainflow on the slipface. (b) Flow field map based upon the wind ripple orientations. White arrows indicate transport directions inferred from wind ripple orientations. Secondary flow configurations based on the wind ripple orientations relative to the primary crestlines are labeled along the primary crestline. (c) Simplified airflow and surface process map based on Figure 11b.

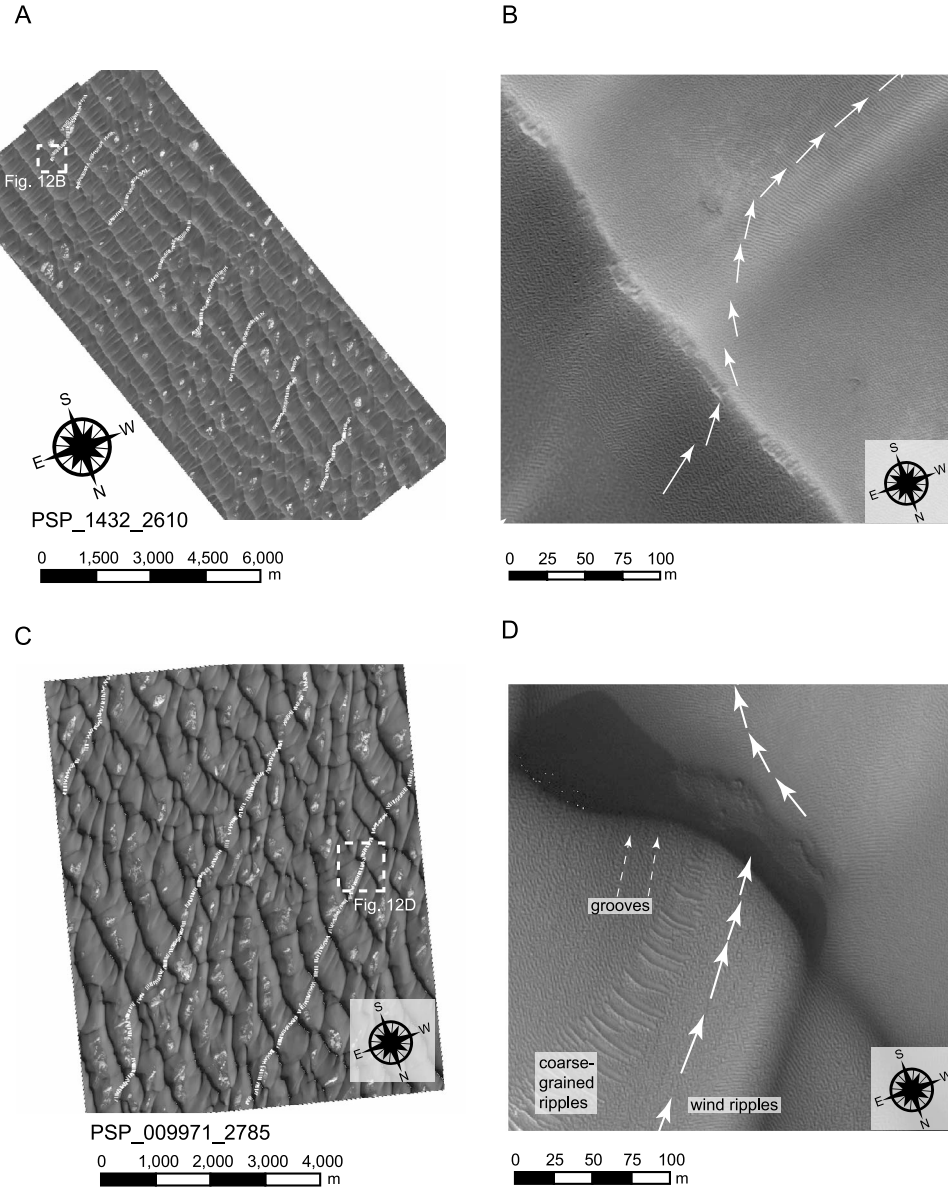


Figure 12. Field-scale flow pathways mapped by ripple orientation along transects from the NE to the SW. (a) Eight flow pathway transects mapped across the center of the study area. (b) Inset showing the flow pathway across a primary and secondary dune crestline within the study area. (c) Three flow pathway transects mapped on HiRISE image PSP_009971_2785, which lies 10 km N of the study area. Lighting is from 044°W longitude. (d) Inset of Figure 12c showing the transport across a crestline. Erosional grooves on the dune stoss slope indicated by dashed white arrows.

primary pattern suggests that it developed during a period in which more sediment was available for aeolian transport (i.e., the dunes were less stabilized), whereas the secondary pattern appears to have developed in a low sediment availability environment following the stabilization of the primary pattern.

6. Determination of Wind Regimes

[38] Given the geomorphic evidence of a complex pattern, within what wind regimes did the pattern arise? What is the most recent wind and does it relate to the pattern formation?

6.1. Determination of Most Recent Flow Fields

[39] Given a crestline orientation determined by the overall wind regime (i.e., the gross bed form-normal orientation) the wind at any 1 time may strike the crestline at any angle, defining the incidence angle. Incidence angles have been defined as transverse (70° – 90°), longitudinal (0 – 10°), or oblique (10° – 70°) [Sweet and Kocurek, 1990]. These incidence angles each define a characteristic secondary flow configuration on the lee face [Sweet and Kocurek, 1990; Walker and Nickling, 2002]. With a longitudinal configuration, flow is attached and transport is along slope. As the

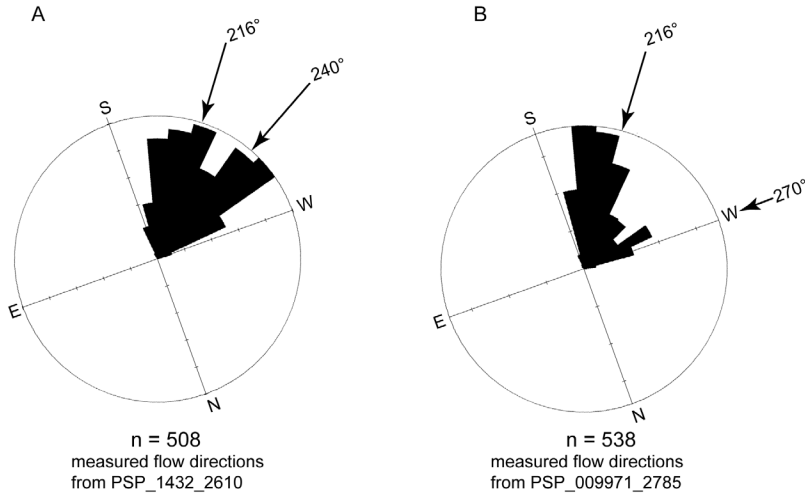


Figure 13. Rose diagrams of the transport directions mapped in (a) the study area and (b) HiRISE image PSP_009971_2785. In Figure 13a, the mode at 216° is perpendicular to the measured ripple and coarse grained ripple orientation (see Figure 9) and the mode at 240° is parallel to the orientation of the secondary dunes. In Figure 13b, a dominate mode occurs near 216° and a subordinate mode near 270°. The consistency of the transport direction toward 216° suggests the last significant transporting wind was from the NE at $\sim 036^\circ$.

incidence angle becomes greater (i.e., oblique) the lee flow is deflected to blow along slope, followed by flow separation in the form of a 3-D vortex with components of along-slope and reversed flow [e.g., Allen, 1982]. A 2-D roller with a crest-normal return flow occurs as the incidence angle approaches 90°.

[40] In turn, the characteristic flow configurations give rise to specific surface processes and resultant lee-face surface features [Hunter, 1977]: (1) grainfall in which grains blown passed the brink settle to the surface in paths modified by turbulence [Nickling *et al.*, 2002], (2) grainflow or avalanching of the depositional grainfall, and (3) wind ripples. Grainfall and grainflow are gravity-driven processes, and their exclusive presence is indicative of a transverse flow configuration. Ripples are indicative of a flow configuration where tractional transport dominates. Both grainfall/grainflow and wind ripples can occur with oblique flow with gravity-dominated processes on the upper lee face yielding down-slope to ripples migrating along slope. Under longitudinal flow, ripples may extend to the brink of the lee face. In total, lee-face surface features are robust indicators of local flow conditions as a function of the incidence angle.

[41] Using the relationship between the dune-modified secondary flow and the resulting surface features, the flow fields within a representative area of the study area were mapped (Figures 11a–11c). The secondary flow configuration interpreted from the ripple crestlines and the occurrence of grainfall (Figures 7c and 11a) is shown in Figure 11b, with the generalized flow field illustrated in Figure 11c. The flow configuration consists of a primary flow from the NE with modified secondary flow over the dune topography. In Figure 11b, flow emerging from a hollow lower on the stoss slope is deflected to the SW in the direction of the primary flow as it approaches the primary crest. At the crest, flow is transverse to the slipface orientation, and longitudinal and oblique along areas without a slipface. In the lee of the lon-

gitudinal and oblique areas, the SW flow is deflected along slope to the S. Approximately 80 m W of the oblique areas of the crestline flow recovers to the primary SW flow direction. At the transition from longitudinal to oblique flow, the grainfall apron appears and widens along-slope southward until it merges with the slipface. Approximately 80 m SW of the slipface flow recovers to the SW, indicating the line of attachment for this separated flow. SW flow crossing the secondary dune crestline is deflected W and contours along the SE facing slope until reaching the next downwind primary crestline. Overall, the structure of the secondary airflow through the field, as inferred from the surface features, is governed by the primary and secondary dunes and indicates that the last transporting wind must have blown from the NE to SW.

[42] The distance from the crestline to the point where the airflow recovers to the primary flow direction depends largely upon dune height and incident angle [Sweet and Kocurek, 1990]. In aeolian systems for both transverse and oblique flows, this distance is 4–8 dune heights downwind of the crest, which corresponds to estimates in fluvial systems [McLean and Smith, 1986] and estimates on Mars [Bourke *et al.*, 2004]. Using this measure, the estimated dune height of the primary dune at this location would be 10–20 m.

6.2. Field-Scale Flow

[43] In order to constrain the prevailing wind direction during the last transport event, flow fields were mapped over multiple dunes in the study area and in HiRISE image PSP_009971_2785, which is 10 km north of the study area (Figures 1 and 12c). Line segments were mapped perpendicular to the ripple orientations along multiple transects from the NE to the SW throughout each area (Figures 12a–12d). Figure 12a shows eight flow path transects across the center portion of the study area. Areas outside the center of the image have a degraded spatial resolution and deter-

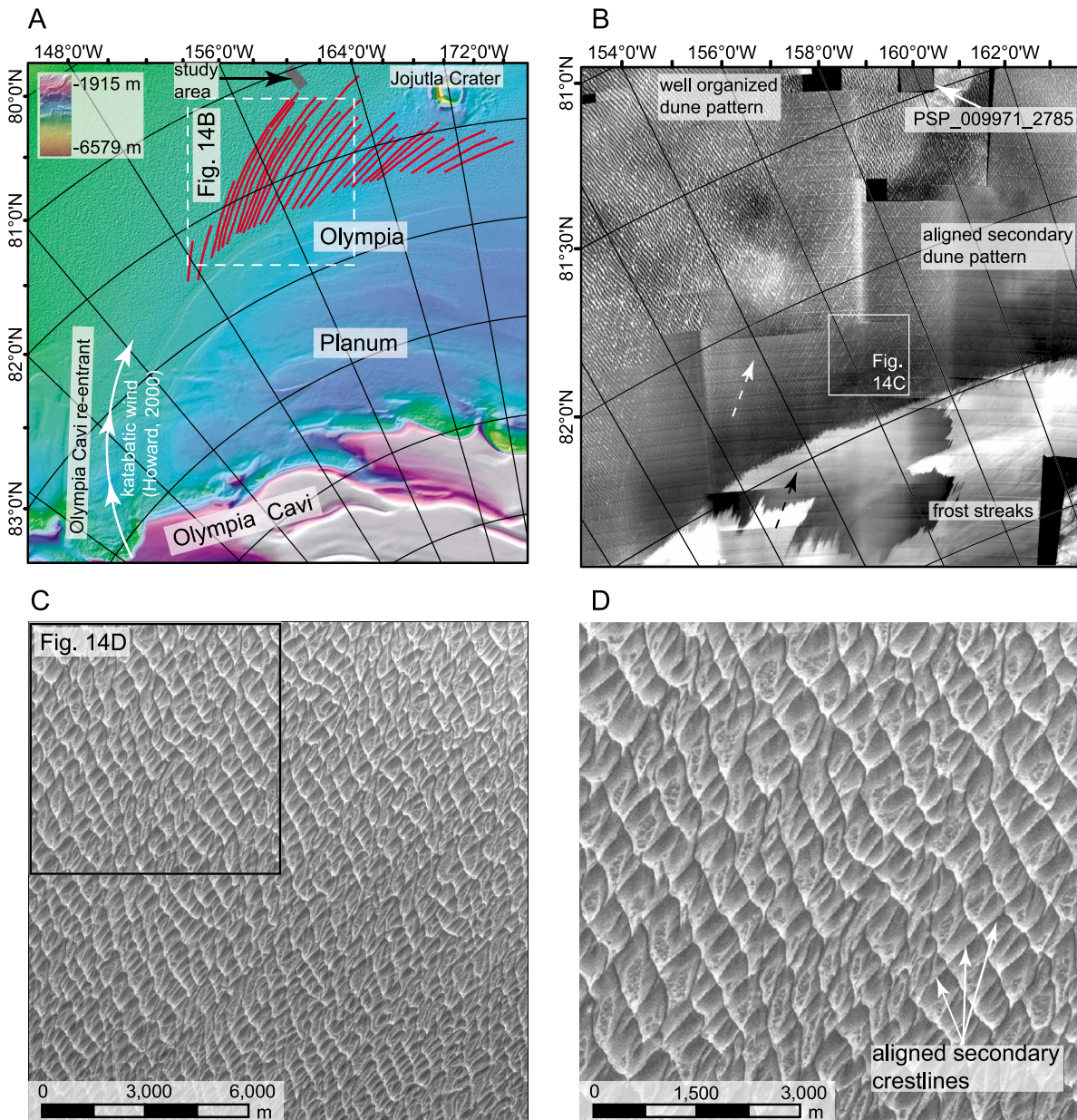


Figure 14. Regional-scale view of the center of the Olympia Undae Dune Field showing an E-W change in the dune field pattern attributed to katabatic winds emerging from the Olympia Cavi reentrant. (a) MOLA DEM with the trends of the secondary crestlines (red) mapped from the THEMIS mosaic shown in Figure 14b. The white arrows denote the trend of the katabatic winds mapped from frost streaks by Howard [2000]. (b) THEMIS mosaic showing the E-W change in the dune field pattern from well-organized crescentic dunes in the E of the reentrant to an aligned secondary dune pattern to the west. Note the alignment of the frost streaks on the planum (noted by the black dashed arrow) with the secondary crestlines (dashed white arrow) in the dune field. (c) Context Camera (CTX, image P13_006153_2608) (NASA/JPL/MSSS) image of subset located in Figure 13b, showing the well-aligned secondary crestlines and an overall star dune type pattern. Note the prominence of the secondary crestlines is equal to that of the primary crestlines, whereas in the study area the secondary crestlines are more subdued. (d) CTX image subset shown in Figure 13c showing in detail the star dune nature of the pattern.

mining the ripple orientation was not possible. The consistent orientation of the paths shows that the general direction of transport is from the NE to the SW, which is in agreement with the detailed mapping discussed above. Figure 12b shows that the transport pathways through the dune field

are controlled by the topography of the primary and secondary crestlines.

[44] Although the dune field pattern in HiRISE image PSP_009971_2785 (Figure 12c) is different from the study area, the flow paths indicate that transport is toward the SW,

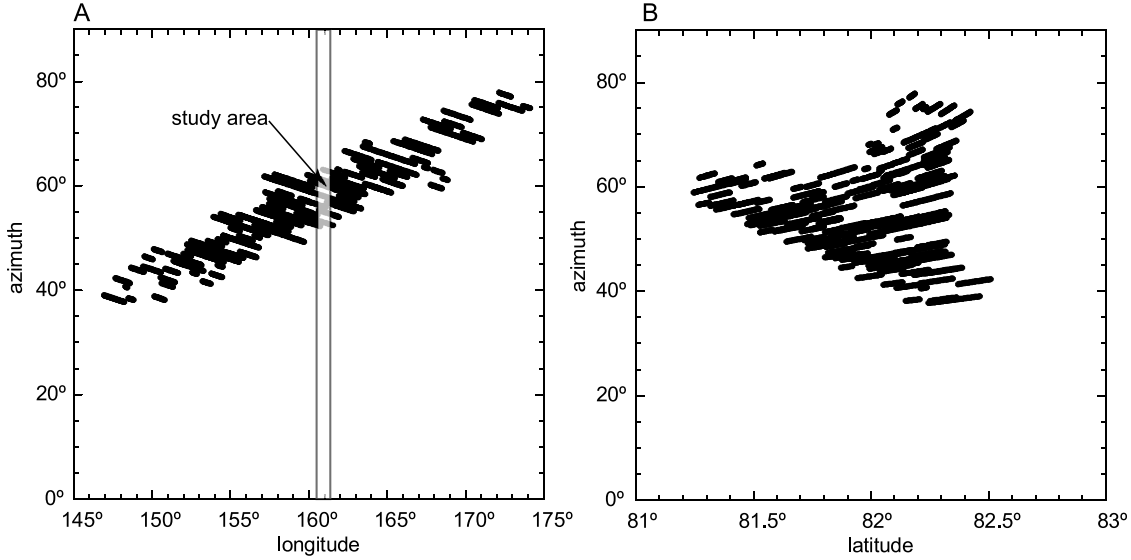


Figure 15. Azimuth versus (a) longitude and (b) latitude plots showing the change in the orientation of the aligned secondary crests westward of the mouth of the Olympia Cavi reentrant (see text for discussion).

as in the study area. The inset image (Figure 12d) shows the alignment of ripples, coarse-grained ripples, and grooved features on the stoss slopes in the transport direction. The grooved features are more apparent in this area than in the study area to the south and have been interpreted as erosion of an indurated surface by aeolian abrasion and plucking [Horgan *et al.*, 2009b].

[45] Flow path vectors from the study area and HiRISE PSP_009971_2785 were plotted on separate rose diagrams to determine the transport direction of the winds that created the ripples (Figure 13). Figure 13a shows a bimodal distribution of transport vectors for the study area. One mode is near 216°, which is perpendicular to the average ripple orientation of 306° (Figure 8e). Another mode occurs near 240°, which parallels the orientation of the secondary crestlines and reflects the transport along the lee slope of these crests. The two modes reflect the typical transport pathway shown in Figure 12b. Figure 13b shows the transport vectors for HiRISE image PSP_009971_2785. A dominate mode occurs near 216° and a much smaller mode occurs near 270°.

[46] Although the transport directions reflect a range of dune-modified airflow, the consistency of transport toward the SW, near 216°, in both areas suggests the last significant transporting wind blew from the NE, ~036°.

7. Pattern Construction

7.1. Pattern Constructional Winds

[47] Theory, models [Tyler and Barnes, 2005], and empirical data [Tsoar *et al.*, 1979; Howard, 2000; Langevin *et al.*, 2005; Tanaka and Hayward, 2008] indicate circumpolar easterly winds are a persistent and dominant part of the wind regime around the north polar ice cap. Although crestline orientation does not necessarily indicate the primary wind direction, the well-organized N-S oriented (342°) crestlines of the primary dune pattern and the above evidence reasonably argue that the primary dune pattern formed transverse to a circumpolar easterly wind. The influence of the NE wind is

not apparent in the older pattern and is not needed to most simply explain the primary dune pattern. Within the study area an easterly wind transverse to the orientation of the primary dunes would be an ENE wind (072°).

[48] In contrast to the simplicity of the primary dune pattern, the secondary crestlines (060°) are highly oblique to the NE (036°) wind and longitudinal to the ENE (072°) wind. Neither of the winds alone explains the orientation of the secondary crestline. However, the secondary crestlines can be well explained as longitudinal elements to the resultant transport direction between both winds, depending on the relative magnitude of each wind (i.e., the R value in gross bed form-normal transport) [Rubin and Hunter, 1987]. The secondary crestlines are longitudinal to the resultant between the ENE (072°) and NE (036°) winds, in which the ENE (072°) has a relative magnitude $\sim 2 \times$ greater than the NE (036°) wind.

[49] The NE wind appears to be related to katabatic winds descending Planum Boreum, which become deflected by Coriolis forcing. Katabatic winds refer to downslope winds. Over large ice sheets such as Greenland and Antarctica, katabatic winds arise from radiational cooling of the ice, which creates strong horizontal pressure gradients between the upland, ice-covered areas and the basinward ice-free area that, along with gravity, drive the cool, dense winds downslope [Parish, 1988]. Similarly, in the north polar region of Mars, katabatic winds are thought to arise from the contrast between the elevated, high-albedo Planum Boreum ice cap and relatively lower-albedo surrounding terrain [Tsoar *et al.*, 1979; Siili *et al.*, 1997; Howard, 2000]. This contrast is thought to be particularly strong during the Martian summer in Olympia Undae when the expanses of low-albedo sands are frost free and warmer than the residual ice cap [Tsoar *et al.*, 1979; Siili *et al.*, 1997; Tyler and Barnes, 2005].

[50] Howard [2000] mapped frost streaks on the Planum Boreum as indicators of katabatic winds and found that katabatic winds follow topography, draining into the major

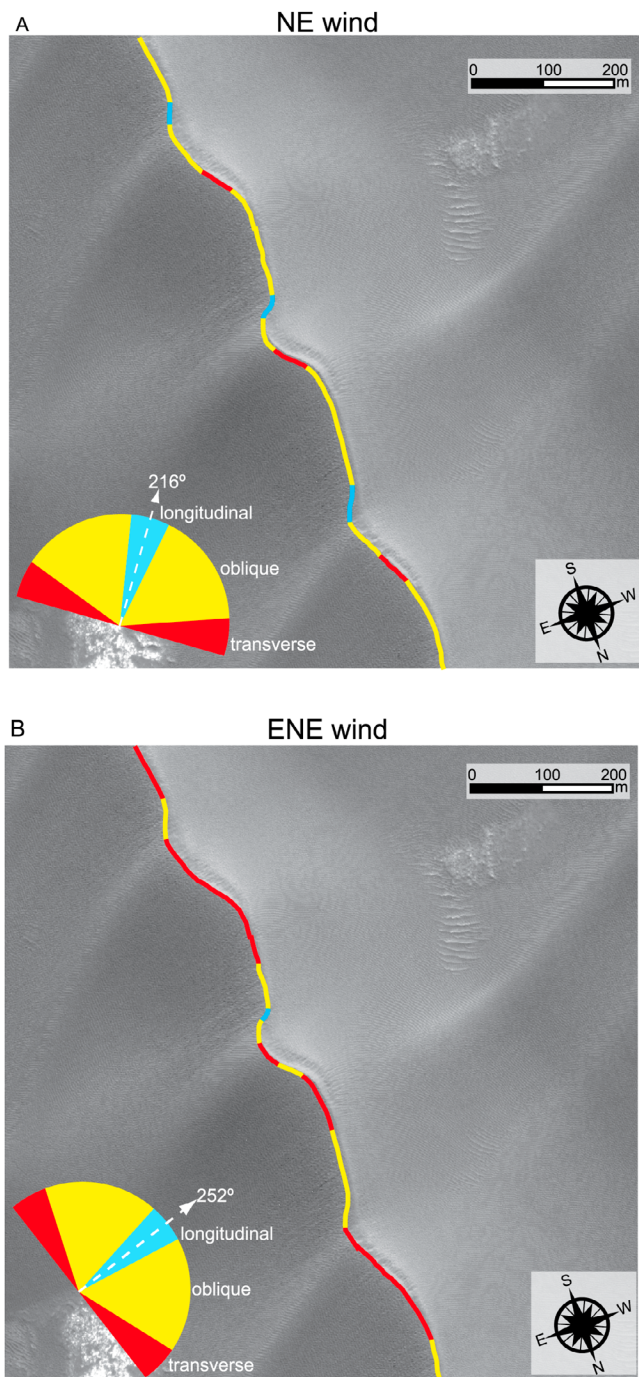


Figure 16. Incident angles shown along a portion of the primary crestlines within the study area for both (a) the NE wind and (b) the ENE wind. Colored areas indicate the incident angle, as defined by Sweet and Kocurek [1990], between the primary crestline and the wind. Red areas are transverse (70° – 90°), yellow areas are oblique (10° – 70°), and blue areas are longitudinal (0° – 10°). In both images, three slipfaces are shown along the primary crest, the middle of which is also shown in Figures 11a and 11b.

chasmae and reentrants of Planum Boreum [see Howard, 2000, Figure 1]. The convergence of katabatic winds within the major drainages is thought to create strong winds, which erode the scarps and layered deposits, and, over the long term, may be a primary mechanism by which the reentrants evolve. Sediment produced from the erosion of the layered deposits is thought to provide sediment to dune fields, which are typically outboard of the reentrants [Howard, 2000; Tanaka *et al.*, 2008]. A large reentrant that extends from the Olympia Cavi escarpment connects Olympia Undae with Planum Boreum and is thought to be a primary drainage of katabatic winds (Figure 14).

[51] A distinct E to W spatial change in the Olympia Undae Dune Field pattern appears to reflect katabatic winds channeled from the Olympia Cavi reentrant (Figure 14). Westward of the reentrant that connects the Olympia Cavi escarpment with Olympia Undae, the secondary crestlines are strongly aligned, arcing out from the base of the Olympia Planum into the field center (Figures 14a–14b). Eastward the primary dunes are dominant and appear as well-organized crescentic dunes (Figures 14a–14b). The secondary crestlines are as prominent as the primary crestlines closer to Planum Boreum (Figures 14c–14d) but become subdued features southward into the field center, as with the secondary crestlines in the study area.

[52] Results from mapping the orientation of the secondary crestlines from the reentrant westward and from the northern margin of the field to the study area (Figure 14a) show that the orientations of the secondary crestlines range from $\sim 40^{\circ}$ at the mouth of the reentrant to $\sim 80^{\circ}$ just north of Jojutla Crater (Figure 15). Whereas the secondary crestline orientations are more dependent on the distance westward from the reentrant rather than the distance from the base of Olympia Planum (Figure 15), the prominence of the secondary crestline depends on distance from Planum Boreum. At the field scale, the alignment and orientation of the secondary dunes appear to reflect the influence of katabatic winds draining from the Olympia Cavi reentrant that are deflected westward around the base of the elevated, northern part of Olympia Planum by Coriolis forcing. The waning prominence of the crestlines southward indicates that the katabatic winds decrease in intensity outward from the Olympia Planum.

[53] Overall, the katabatic winds appear to be the most recent winds and related to the development of the second generation of dunes within the Olympia Undae Dune Field. The appearance of these winds as an influence on the dune field pattern may have initiated with the erosion and retreat of the Olympia Cavi reentrant. The development of this reentrant would have channeled katabatic winds descending Planum Boreum, as well as injected into Olympia Undae a new supply of sediment derived from the erosion of the sedimentary units underlying Planum Boreum.

7.2. Crestline Dynamics During Constructional Winds

[54] Mapping incident angles and the resulting secondary flow patterns [cf., Sweet and Kocurek, 1990] between the primary dune crestline and the NE wind and the ENE wind provide a basis for a model of the development of the secondary crestline pattern and the current state of dune field evolution. Figure 16a shows three slipfaces along a primary crestline with the secondary flow configuration illustrated for the NE wind. The center slipface is shown in more detail

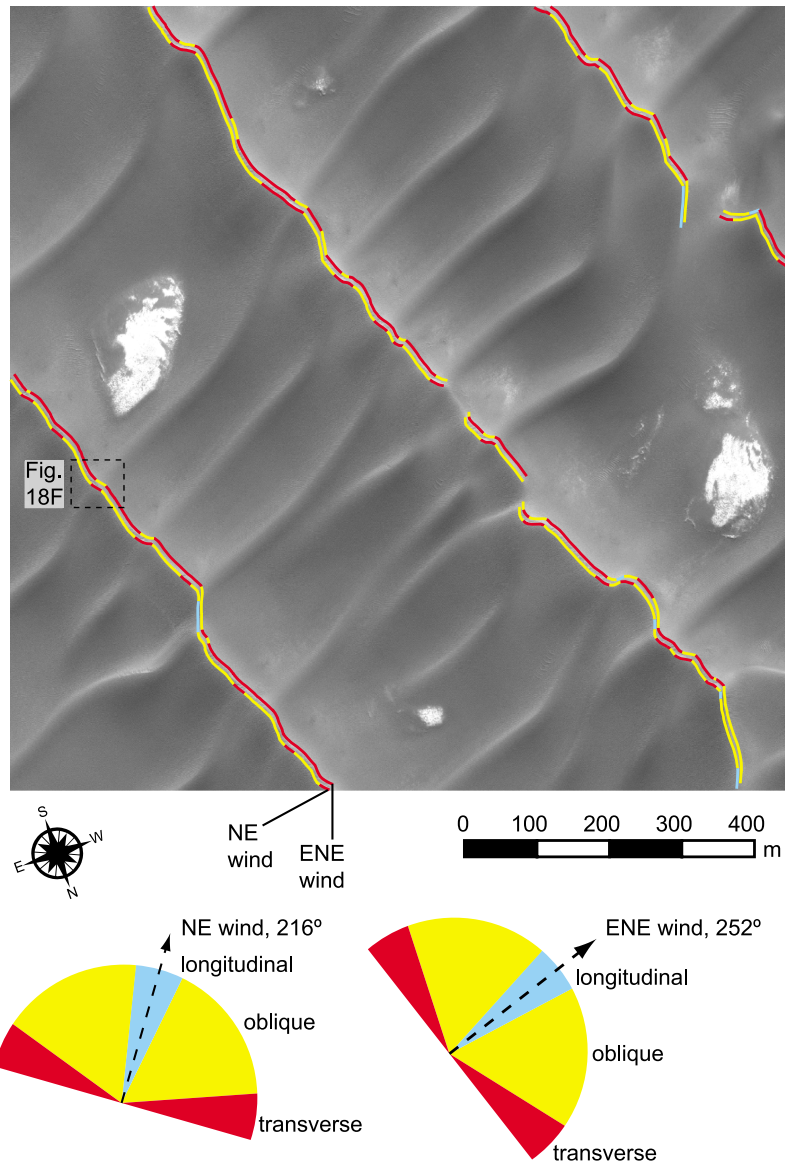


Figure 17. Incident angle map with both the incident angles for the NE and the ENE winds side-by-side along the primary crestlines (see text for discussion).

in Figures 11a–11b. The most developed areas of the slipfaces consistently occur along areas that are transverse (red) to the NE wind. The flanks of the slipfaces are commonly oblique (yellow) to the NE wind and extend into stretches of subdued, wind-rippled crestral areas that occupy much of the

area between the slipfaces. Short pieces of crestline south of the slipfaces are longitudinal to the NE wind. Sediment transported through the secondary flow fields created by the NE wind would move southward along-slope until reaching a region of increasing flow deceleration and deposition,

Figure 18. Model of slipface development and primary crestline segmentation based upon the relationship between the primary crestline and secondary crestline within the bimodal wind regime. (a) Development of a slipface on the primary crestline arising from the secondary flow configuration determined by the interaction of the primary and secondary dune topography under the NE wind. Lines indicate relative amount of deposition, with maximum deposition (i.e., longer lines) occurring at the most transverse portions of the crestline and less deposition as flow becomes more oblique. (b) Creation of a convex nose at the focal point of deposition that becomes transverse to the NE wind. (c) Influence of the ENE wind when the SE flank of the convexity becomes oblique ($\sim 20^\circ$) to this wind. Flow is deflected NW toward the transverse areas at the nose of the convexity. (d) Renewal of the NE wind and continued progradation and segmentation of the primary crestline. (e) Side-by-side flow configurations for both the NE and ENE winds, as in Figure 17. Note the reciprocal flow configuration along the slipface that creates a point of maximum deposition at the nose of the convexity. As shown in Figure 18F, this flow configuration coincides with a downwind secondary dune.

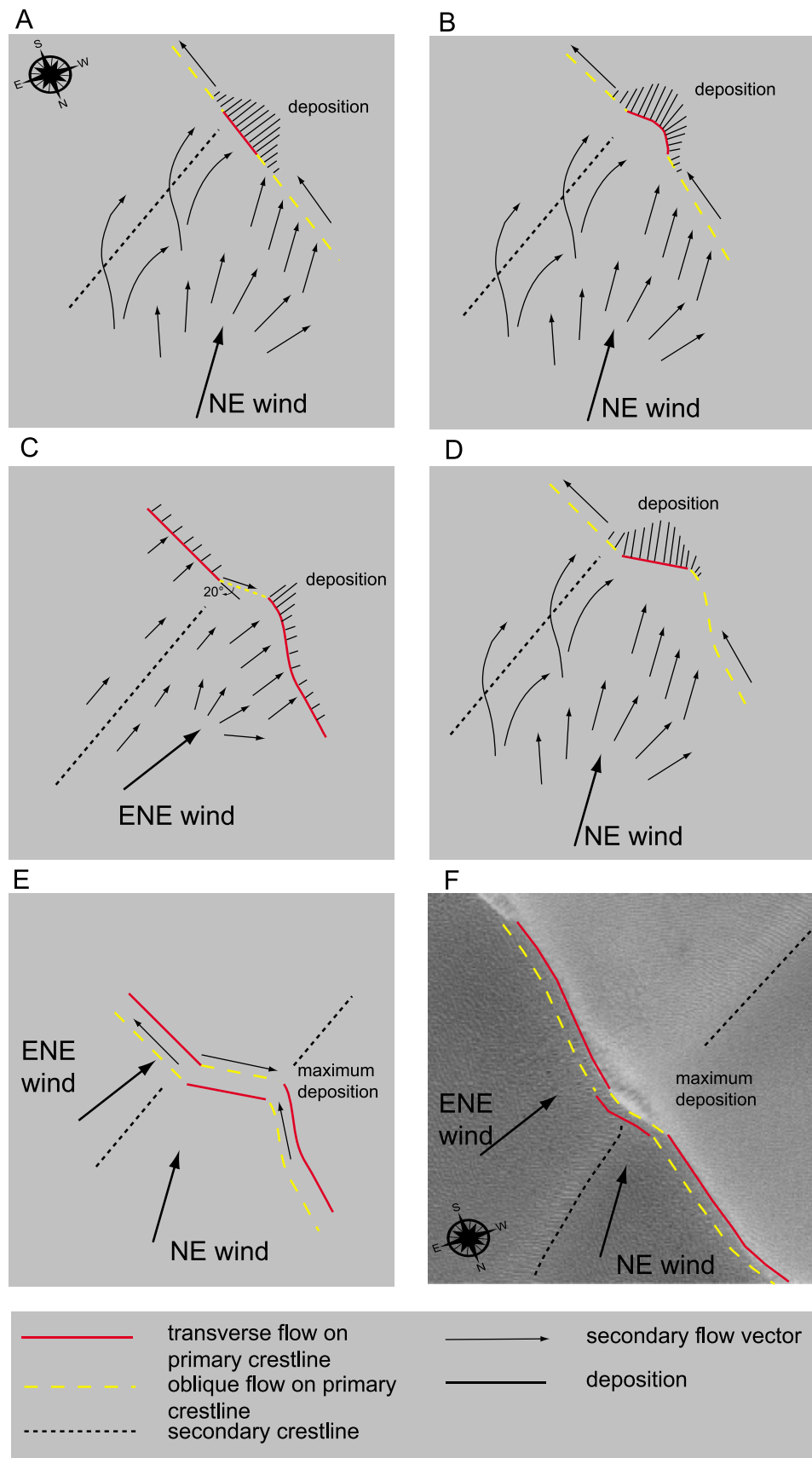


Figure 18

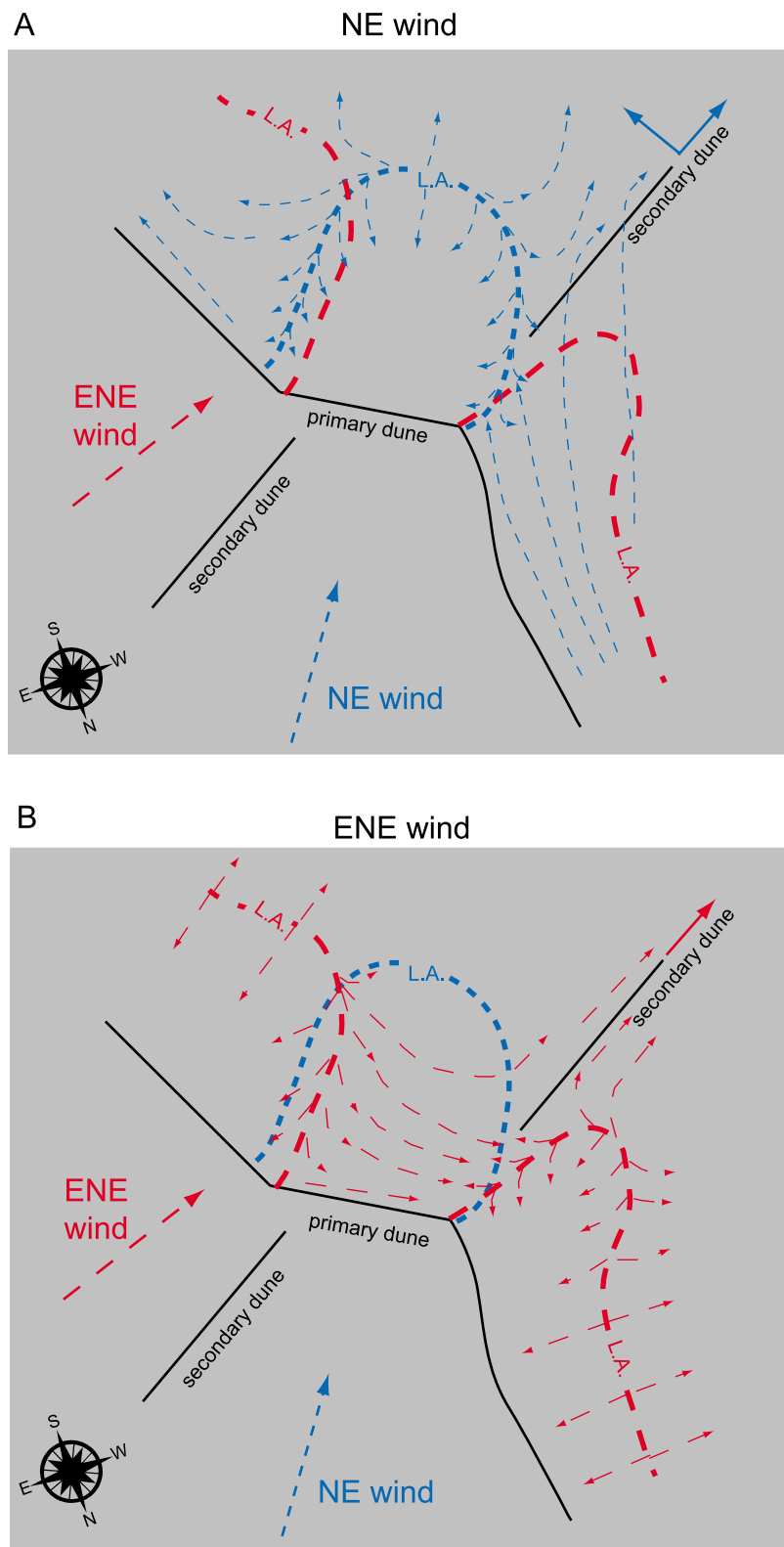


Figure 19

with maximum deposition at the transverse portions of the crestline.

[55] Figure 16b shows the incident angles for the ENE wind. In contrast to the NE wind, much of the primary crestline is transverse to this wind. Sediment transported under the ENE secondary flow field would be deposited lee of the transverse crestral areas and move southward along-slope through the oblique and longitudinal areas. An exception to this occurs along the oblique portion of the crest in the center of the middle slipface where sediment would move NW with deposition occurring at the high-angle oblique and transverse areas.

[56] Figure 17 shows secondary flow configurations in the area of the field shown in Figure 3a. The crestral areas transverse to the NE wind are nearly always coincident with the slipfaces, but overall most of the primary crestline is oblique to this wind. With the ENE wind, most of the crestline is transverse and punctuated by small segments of oblique flow. A side-by-side comparison of the flow configurations for both winds (Figure 17) shows that secondary crestlines start in the interdune areas downwind of slipfaces that are transverse to the NE wind and oblique to the ENE wind.

[57] The occurrence of the most developed slipfaces transverse to the NE wind, the active-appearing ripples in the lee of the secondary dunes, and the potential sediment influx from the katabatic winds all suggest that the NE wind introduces more sediment to the dune field than the ENE wind, although both winds are likely highly undersaturated because of frozen dune conditions. If the ENE wind carried a significant amount of sand, well-developed slipfaces should appear transverse to these winds, rather both slipfaces and wind-rippled crestlines are transverse to the ENE wind. The secondary flow fields and geomorphic evidence suggest that much of the sediment supply entering the field within the study area likely derives from the NE wind, whereas the ENE wind acts to only move sediment deposited by the NE wind.

7.3. Model of Pattern Construction

[58] The relationship between the inferred flow pathways, incident angles, and dune topography provides the basis for a model of the development of the dune field pattern to its current state. Within this model, the interaction between the primary and secondary dunes within the bimodal wind regime creates a feedback in which the primary crestline is segmented and reoriented, and the secondary crestline is propagated in the resultant flow direction (Figures 18 and 19).

[59] Resulting from the interactions between the primary and secondary crestlines is the formation and progradation of a convex nose along the primary crestline (Figures 18a and 18b). This convex nose is an emergent pattern feature arising because of the development of the secondary dunes upon the antecedent primary dune topography. The net effect of the development of the convex nose on the pattern is the reorientation and segmentation of the primary dune. Geomorphically, this is evident as dislocations along the primary crestline (Figures 3a, 7b, and 18f). This segmentation is the process of pattern reformation within the new wind regime and the development of a complex pattern.

[60] The process that breaks up the primary crestlines also establishes a secondary flow configuration that focuses deposition along the primary dune lee slope and initiates the development of a secondary dune (Figure 19). This occurs in a manner similar to the formation of linear dunes in a bimodal wind regime, but in this case as secondary flow on the plinth of the primary crests during the bimodal wind regime. With the elongation of the secondary dune under the NE wind (Figures 19a and 20) and ENE wind (Figure 19b) the secondary crestline can extend to the next dune downwind, with the formative process repeated, thus giving rise to the reticulate pattern.

8. Conclusions

[61] The dune field pattern in one area of the Olympia Undae Dune Field was analyzed via measurements and statistical analysis of the pattern elements, and the flow field was reconstructed based upon wind ripples formed during the most recent transporting winds. Pattern analysis and geomorphic relationships show a complex pattern in which older, well-organized NNW oriented dunes are being reworked by younger, NE oriented dunes. Mapped flow fields indicate that the most recent transporting winds were from the NE and are likely related to katabatic winds descending Planum Boreum through the Olympia Cavi reentrant.

[62] Within the general context of dune field pattern formation, the scenario of pattern reformation with the onset of a changed wind regime is well illustrated with this Martian example. First, the position and development of the secondary dunes is controlled by the boundary condition of the antecedent primary dune topography. In the absence of this boundary condition the longitudinal secondary dunes would be expected to be unstable under this wind regime and would destabilize into trains of barchans. Rather, they reach

Figure 19. Details of the secondary flow configuration occurring along the primary dune plinth that gives rise to the initiation, elongation, and migration of the secondary dunes. (a) Flow configuration for the NE winds. (b) Flow configuration for the ENE winds. The secondary dune initiates where secondary flow from the bimodal wind regime converges on the dune plinth creating a focal line of deposition. The thick dashed lines are lines of attachment (L.A.) defining the separation cell in the lee of the transverse portions of the crestline for both (a) the NE (blue) and (b) the ENE (red) winds. This area bound by the attachment line is well defined for the NE wind by the mottled ripples in the lee of the slipface shown in Figures 11a and 11b. The dashed arrows represent inferred secondary flow vectors for the NE (blue) and ENE (red) winds. Return flow (i.e., flow inside the attachment line) moves directly back toward the crestline along the most transverse portions of the separation cell and sweeps inward toward the crest along the oblique regions. Outboard of the attachment line, flow returns to the primary flow direction or becomes incorporated into secondary flow along the primary or secondary dune. The solid blue arrows in Figure 19a indicate the WSW elongation and SE migration of the secondary dune under the NE wind. The solid red arrow at the end of the downwind secondary dune in Figure 19b indicates the WSW elongation of the secondary dune under the ENE wind.

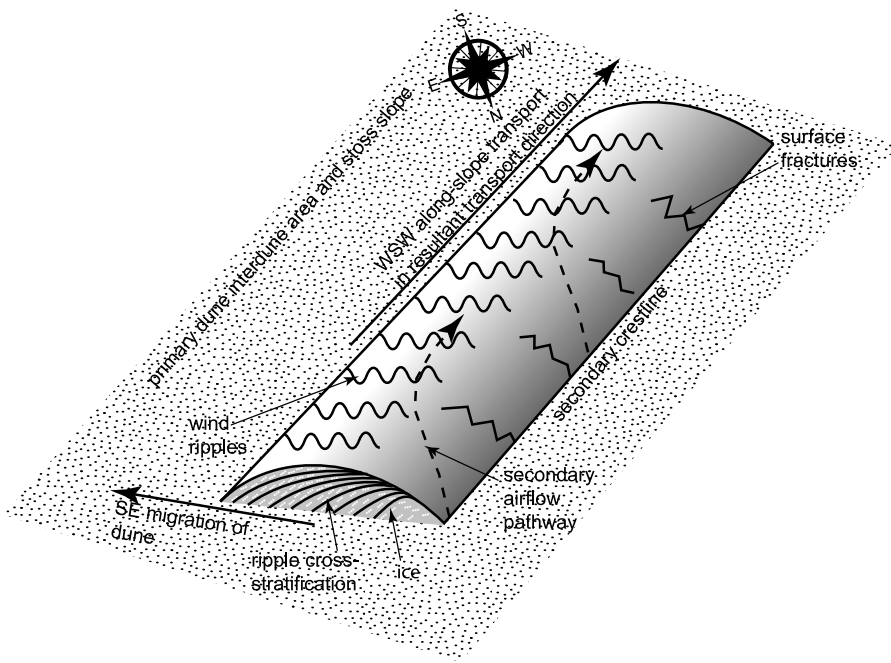


Figure 20. Model of the WSW elongation and SE migration of the secondary dunes by wind ripple migration along the SE slope of the dune. Wind ripple migration on the SE facing slope arises from NE flow that becomes deflected to the WSW as it crosses the secondary dune crestline and from longitudinal flow from the ENE winds. Elongation occurs with WSW along-slope sediment transport. SE migration of the dune occurs through sediment accumulation on the SE facing slope, which is the depositional slope of the dune under the NE winds. In cross-section the SE migration would be apparent by wind ripple stratification dipping to the SE.

a downwind primary crest before destabilization can occur. Second, it shows the development of a complex pattern through dune interactions between pattern generations (i.e., the younger secondary dunes intersecting the older primary dunes), as well as the reformation of the older pattern with their breakup by the secondary dunes. Third, the secondary flow field that allows for the reformation of the field arises because of the interactions between the dune generations.

[63] **Acknowledgments.** Funding provided by NASA MDAP NNX07AV36G. Comments from Douglas J. Jerolmack and an anonymous reviewer are gratefully acknowledged.

References

- Aharonson, O., and N. Schorghofer (2006), Subsurface ice on Mars with rough topography, *J. Geophys. Res.*, 111, E11007, doi:10.1029/2005JE002636.
- Allen, J. R. L. (1982), *Sedimentary Structures: Their Character and Physical Basis. Developments in Sedimentology*, 30A, 593 pp., Elsevier, Amsterdam.
- Bagnold, R. A. (1941), *The Physics of Blown Sand and Desert Dunes*, 265 pp., Methuen, London.
- Bandfield, J., V. Hamilton, and P. Christensen (2000), A global view of Martian surface compositions from MGS-TES, *Science*, 287, 1626–1630, doi:10.1126.
- Beveridge, C., G. Kocurek, R. C. Ewing, N. Lancaster, P. Morthekai, A. K. Singhvi and S. A. Mahan (2006), Development of spatially diverse and complex dune field patterns: Gran Desierto Dune Field, Sonora, Mexico, *Sedimentology*, 53, 1391–1409, doi:10.1111/j.1365-3091.2006.00814.x.
- Bourke, M. C., J. E. Bullard, and O. S. Barnouin-Jha (2004), Aeolian sediment transport pathways and aerodynamics at troughs on Mars, *J. Geophys. Res.*, 109, E07005, doi:10.1029/2003JE002155.
- Bourke, M. C., M. Balme, R. A. Beyer, K. K. Williams, and J. Zimbelman (2006), A comparison of methods used to constrain the height of sand dunes on Mars, *Geomorphology*, 81, 440–452, doi:10.1016/j.geomorph.2006.04.023.
- Bourke, M. C., K. S. Edgett, and B. A. Cantor (2008), Recent aeolian dune change on Mars, *Geomorphology*, 94, 247–255, doi:10.1016/j.geomorph.2007.05.012.
- Bourke, M. C., A. Philippoff, and N. Bridges (2009), Studies of dune change on Mars combining MOC and HiRISE images: *Lunar Planet Sci.*, XL, Abstract 1748.
- Breed, C. S., M. J. Grolier, and J. F. McCauley (1979), Morphology and distribution of common “sand” dunes on Mars: Comparison with Earth, *J. Geophys. Res.*, 84(B14), 8183–8204.
- Byrne, S., and B. Murray (2002), North polar stratigraphy and the paleo-erg of Mars, *J. Geophys. Res.*, 107(E6), 5044, doi:10.1029/2001JE001615.
- Derickson, D., G. Kocurek, R. C. Ewing, and C. Bristow (2008), Origin of a complex and spatially diverse dune field pattern, Algodones, southeastern California, *Geomorphology*, 99, 186–204, doi:10.1016/j.geomorph.2007.10.016.
- Ewing, R. C., and G. Kocurek (2010a), Aeolian dune field pattern boundary conditions, *Geomorphology*, 114, 175–187, doi:10.1016/j.geomorph.2009.06.015.
- Ewing, R. C., and G. Kocurek (2010b), Aeolian dune interactions and dune field pattern formation: White Sands Dune Field, New Mexico, *Sedimentology*, 57, 1199–1219, doi:10.1111/j.1365-3091.2009.01143.x.
- Ewing, R. C., G. Kocurek, and L. W. Lake (2006), Pattern analysis of dune field parameters, *Earth Surf. Process. Landforms*, 31, 1176–1191, doi:10.1002/esp.1312.
- Feldman, W. C., M. C. Bourke, R. C. Elphic, S. Maurice, J. Bandfield, T. H. Prettyman, B. Diez, and D. J. Lawrence (2008), Hydrogen content of sand dunes within Olympia Undae, *Icarus*, 196, 422–432, doi:10.1016/j.icarus.2007.08.044.
- Fishbaugh, K., and J. Head III (2005), Origin and characteristics of the Mars north polar basal unit and implications for polar geologic history, *Icarus*, 174, 444–474, doi:10.1016/j.icarus.2004.06.021.
- Fishbaugh, K. E., F. Poulet, V. Chevrier, Y. Langevin, and J. P. Bibring (2007), On the origin of gypsum in the Mars north polar region, *J. Geophys. Res.*, 112, E07002, doi:10.1029/2006JE002862.

- Fryberger, S. G., P. Hesp, and K. Hastings (1992), Aeolian granule ripple deposits, Namibia, *Sedimentology*, **39**, 319–331.
- Hayward, R. K., K. F. Mullins, L. K. Fenton, T. M. Hare, T. N. Titus, M. C. Bourke, A. Colaprete, and P. R. Christensen (2007), Mars Global Digital Dune Database and initial science results, *J. Geophys. Res.*, **112**, E11007, doi:10.1029/2007JE002943.
- Herkenhoff, K. E., S. Byrne, P. S. Russel, K. E. Fishbaugh, and A. S. McEwen (2007), Meter-scale morphology of the north polar region of Mars, *Science*, **317**, 1711–1715, doi:10.1126/science.1143544.
- Horgan, B. H., J. F. Bell III, E. Z. N. Dobrea, E. A. Cloutis, D. T. Bailey, M. A. Craig, L. H. Roach, and J. F. Mustard (2009a), Distribution of hydrated minerals in the north polar region of Mars, *J. Geophys. Res.*, **114**, E01005, doi:10.1029/2008JE003187.
- Horgan, B., J. Bell, and M. C. Bourke (2009b), A search for dune induration and activity in the north polar region of Mars, paper presented at 7th International Conference on Geomorphology, Eur. Space Agency, Melbourne, Australia.
- Howard, A. D. (2000), The role of eolian processes in forming surface features of the Martian Polar Layered Deposits, *Icarus*, **144**, 267–288, doi:10.1006/icar.1999.6305.
- Hunter, R. E. (1977), Basic types of stratification in small eolian dunes, *Sedimentology*, **24**, 361–387.
- Hunter, R. E., B. M. Richmond, and T. R. Alpha (1983), Storm-controlled oblique dunes of the Oregon coast, *Geol. Soc. Am. Bull.*, **94**, 1450–1465.
- Iverson, J. D., and B. R. White (1982), Saltation threshold on Earth, Mars and Venus, *Sedimentology*, **29**, 111–119.
- Jerolmack, D. J., D. Mohrig, J. P. Grotzinger, D. A. Fike, and W. A. Watters (2006), Spatial grain size sorting in eolian ripples and estimation of wind conditions on planetary surfaces: application to Meridiani Planum, Mars, *J. Geophys. Res.*, **111**, E12S02, doi:10.1029/2005JE002544.
- Kocurek, G., and R. C. Ewing (2005), Aeolian dune field self-organization – Implications for the formation of simple versus complex dune field patterns, *Geomorphology*, **72**, 94–105, doi:10.1016/j.geomorph.2005.05.005.
- Kocurek, G., M. Townsley, E. Yeh, K. Havholm, and M. L. Sweet (1992), Dune and dune-field development on Padre Island, Texas, with implications for interdune deposition and water-table-controlled accumulation, *J. Sediment. Petrol.*, **62**, 622–635.
- Kocurek, G., R. C. Ewing, and D. Mohrig (2010), How do bed form patterns arise? New views on the role of bed form interactions within a set of boundary conditions, *Earth Surf. Processes Landforms*, **35**, 51–63, doi:10.1002/esp.1913.
- Lahtela, H., et al. (2009), Coordinated HiRISE/CRISM Observation on Gypsum Signature in Martian Polar Dunes, in Lunar and Planetary Institute Science Conference Abstracts, pp. 2254.
- Lancaster, N., and R. Greeley (1990), Sediment volume in the North Polar Sand Seas of Mars, *J. Geophys. Res.*, **95**(B7), 10,921–10,927.
- Lancaster, N., G. Kocurek, A. Singhvi, V. Pandey, M. Deynoux, J. F. Ghienne, and K. Lo (2002), Late Pleistocene and Holocene dune activity and wind regimes in the western Sahara Desert of Mauritania, *Geology*, **30**, 991–994, doi:10.1130/0091-7613(2002)030<0991:LPAHDA>2.0.CO.
- Langevin, Y., F. Poulet, J. P. Bibring, and B. Gondet (2005), Sulfates in the north polar region of Mars detected by OMEGA/Mars Express, *Science*, **307**, 1584–1586, doi:10.1126/science.1109091.
- McEwen, A. S., et al. (2007), Mars Reconnaissance Orbiter's High Resolution Imaging Science Experiment (HiRISE), *J. Geophys. Res.*, **112**, E05S02, doi:10.1029/2005JE002605.
- McLean, S. R., and J. D. Smith (1986), A model for flow over two-dimensional bed forms, *J. Hydraul. Eng.*, **112**, 300–317.
- Nickling, W. G., C. McKenna Neuman, and N. Lancaster (2002), Grainfall processes in the lee of transverse dunes, Silver Peak, Nevada, *Sedimentology*, **49**, 191–209, doi:10.1046/j.1365-3091.2002.00443.x.
- Parish, T. R. (1988), Surface winds over the Antarctic continent: A Review, *Rev. Geophys.*, **26**(1), 169–180.
- Roach, L., et al. (2007), CRISM spectral signatures of the north polar gypsum dunes, *Lunar Planet. Sci.*, **XXXVII**, Abstract 1970.
- Rubin, D. M., and R. E. Hunter (1987), Bedform alignment in directionally varying flows, *Science*, **237**(4812), 276–278.
- Schatz, V., H. Tsoar, K. S. Edgett, E. Parteli, and H. J. Herrmann (2006), Evidence for indurated sand dunes in the Martian north polar region, *J. Geophys. Res.*, **111**, E04006, doi:10.1029/2005JE002514.
- Sili, T., R. M. Haberle, and J. R. Murphy (1997), Sensitivity of martian southern polar cap edge winds and surface stresses to dust optical thickness and the large-scale sublimation flow, *Adv. Space Res.*, **19**, 1241–1244.
- Sinclair, A. J. (1976), Applications of probability graphs in mineral exploration, *Assoc. of Exploration Geochemists*, special volume 4.
- Sweet, M. L., and G. Kocurek (1990), An empirical model of aeolian dune lee-face airflow, *Sedimentology*, **37**, 1023–1038.
- Tanaka, K. L., and R. K. Hayward (2008), Mars' north circumpolar dunes: distribution, sources, and migration history, in *Planetary Dunes Workshop: A Record of Climate Change*, p. 69–70. LPI Contribution 1403, Lunar and Planetary Institute, Houston.
- Tanaka, K., J. A. Skinner, and T. M. Hare (2005), Geologic map of the northern plains of Mars. U.S. Geol. Surv. Sci. Invest. Ser. Map SIM-2888.
- Tanaka, K. L., J. A. P. Rodriguez, J. A. Skinner, M. C. Bourke, C. M. Fortezzo, K. E. Herkenhoff, E. J. Kolb, and C. H. Okubo (2008), North Polar region of Mars: Advances in stratigraphy, structure, and erosional modification, *Icarus*, **196**, 318–358, doi:10.1016/j.icarus.2008.01.021.
- Tsoar, H., R. Greeley, and A. R. Peterfreund (1979), Mars: The North Polar Sand Sea and related wind patterns, *J. Geophys. Res.*, **84**(B14), 8167–8180.
- Tyler, D., and J. R. Barnes (2005), A mesoscale model study of summertime atmospheric circulations in the north polar region of Mars, *J. Geophys. Res.*, **110**, E06007, doi:10.1029/2004JE002356.
- Walker, I. J., and W. G. Nickling (2002), Dynamics of secondary airflow and sediment transport over and in the lee of transverse dunes, *Prog. Phys. Geogr.*, **26**(1), 47–75.
- Werner, B. T. (1999), Complexity in natural landform patterns, *Science*, **284**, 102–104, doi:10.1126/science.284.5411.102.
- Werner, B. T. (2003), Modeling landforms as self-organized, hierarchical dynamical systems, in *Prediction in Geomorphology*, edited by P. R. Wilcock and R. M. Iverson, *Geophys. Monogr.*, vol. 135, pp. 133–150, AGU, Washington D. C.
- Werner, B. T., and G. Kocurek (1997), Bedform dynamics: Does the tail wag the dog?, *Geology*, **25**(9), 771–774.
- Werner, B. T., and G. Kocurek (1999), Bedform spacing from defect dynamics, *Geology*, **27**(8), 727–730.
- Wyatt, M., H. McSween, K. Tanaka, and J. Head (2004), Global geologic context for rock types and surface alteration on Mars, *Geology*, **32**, 645–648.
- Zimbelman, J. R. (2010), Transverse aeolian ridges on Mars: First results from HiRISE images, *Geomorphology*, **121**, 22–29, doi:10.1016/j.geomorph.2009.05.012.

M. Bourke, Planetary Science Institute, 1700 E. Fort Lowell, Suite 106, Tucson, AZ 85719-2395, USA.

R. C. Ewing, Division of Geological and Planetary Sciences, California Institute of Technology, Pasadena, CA 91125, USA. (ryancewing@gmail.com)

G. Kocurek and A.-P. B. Peyret, Department of Geological Sciences, The University of Texas at Austin, 1 University Station C9000, Austin, TX 78712, USA.